The Composition of ˜96 keV W+ in Saturn's Magnetosphere

Stephen Christon[1,1], Robert DiFabio[2,2], Douglas Hamilton[3,3], Donald Mitchell[4,4], and Tom Krimigis[4,4]

[1]Focused Analysis & Research
[2]University of Maryland. University of Louisiana
[3]University of Maryland
[4]JHU/APL

November 30, 2022

Abstract

The plumes of Enceladus produce a cloud of neutral H2O molecules and, via dissociation, OH and O. These neutrals are ionized by charge exchange, solar UV, and electron impacts, producing the thermal water group ions W+ (O+, OH+, H2O+, and H3O+) which become energized in Saturn's magnetosphere. We first separate the components of energetic (˜96 keV) W+ using Cassini Charge-Energy-Mass Spectrometer (CHEMS) data from 78 near equatorial main ring current passes (dipole L = 7-16, ±10° in latitude) in 2004-2010. We find ˜53% O+, ˜22% OH+, ˜22% H2O+, and ˜3% H3O+ when averaged over L = 7-16, resulting in a mean water group mass of 16.7 amu. At 7 < L < 21, we find abundance ratios for O+/W+, OH+/W+, and H2O+/W+ that vary little with L. However, while H3O+/W+ is nearly constant at L > 13, H3O+/W+ tends to increase persistently at L < ˜10. The large O+ abundance qualitatively agrees with the broad atomic O cloud observed by Cassini and predicted by some models. Our observation of H2O+/W+ > ˜20% out to L ˜ 21 suggests that neutral H2O spreads throughout the magnetosphere rather than being confined to a narrow H2O torus centered on Enceladus' orbit.

The Composition of ~96 keV W^+ in Saturn's Magnetosphere

R. D. DiFabio[1,2], D. C. Hamilton[1], S. P. Christon[3*], D. G. Mitchell[4], S. M. Krimigis[4,5]

1. University of Maryland, Department of Physics, College Park, MD, USA
2. University of Louisiana, Department of Physics, Lafayette, LA, USA
3. Focused Analysis and Research, Charleston, SC, USA
4. Johns Hopkins University, Applied Physics Laboratory, Laurel, MD, USA
5. Academy of Athens, Athens, Greece

*Corresponding author: S.P. Christon, spchriston@aol.com

Key Points:

- On average, for ~96 keV ions, fractional abundances at L = 7-16 are $O^+/W^+ \sim 0.53$, $OH^+/W^+ \sim 0.22$, $H_2O^+/W^+ \sim 0.\ 22$, and $H_3O^+/W^+ \sim 0.03$
- The partial number densities O^+, OH^+, H_2O^+ and H_3O^+, peak at dipole L ~ 9.5 and the ratios O^+/W^+, OH^+/W^+, and H_2O^+/W^+ vary little with L
- At L < 13, H_3O^+/W^+ decreases significantly with increasing L, whereas at L > 13 H_3O^+/W^+ varies little with L

Abstract

The plumes of Enceladus produce a cloud of neutral H_2O molecules and, via dissociation, OH and O. These neutrals are ionized by charge exchange, solar UV, and electron impacts, producing the thermal water group ions W^+ (O^+, OH^+, H_2O^+, and H_3O^+) which become energized in Saturn's magnetosphere. We first separate the components of energetic (~96 keV) W^+ using Cassini Charge-Energy-Mass Spectrometer (CHEMS) data from 78 near equatorial main ring current passes (dipole L = 7-16, ±10° in latitude) in 2004-2010. We find ~53% O^+, ~22% OH^+, ~22% H_2O^+, and ~3% H_3O^+ when averaged over L = 7-16, resulting in a mean water group mass of 16.7 amu. At 7 < L < 21, we find abundance ratios for O^+/W^+, OH^+/W^+, and H_2O^+/W^+ that vary little with L. However, while H_3O^+/W^+ is nearly constant at L > 13, H_3O^+/W^+ tends to increase persistently at L < ~10. The large O^+ abundance qualitatively agrees with the broad atomic O cloud observed by Cassini and predicted by some models. Our observation of H_2O^+/W^+ > ~20% out to L ~ 21 suggests that neutral H_2O spreads throughout the magnetosphere rather than being confined to a narrow H_2O torus centered on Enceladus' orbit.

Introduction

[1] The discovery of OH in Saturn's magnetosphere by the Hubble Space Telescope (HST) indicated that Saturn's magnetosphere contains a significant source of neutral H_2O (Shemansky et al., 1993). Using Voyager and HST observations, Jurac and Richardson (2005) modeled the plasma and neutral particles in Saturn's magnetosphere and predicted that the majority of the H_2O was coming from Enceladus at a rate of ~10^{28} H_2O/s, a small moon at ~4 R_S (the Saturn radius; please note that near the equator, dipole L = 1 is about 1 R_S). The discovery of water plumes in the south-pole region of Enceladus by the Cassini mission confirmed their predictions (Waite et al., 2006; Hansen et al., 2006; Porco et al., 2006). Typical estimates of the plume source strength range from ~1-4x10^{28} H_2O/s (Burger et al., 2007; Jia et al., 2010; Dong et al., 2011), but some studies suggest that the source strength varies significantly with time and can be as low as ~0.6-0.7x10^{28} H_2O/s (Saur et al., 2008; Smith et al., 2010). Cassini measurements of the ionized H_2O products (O^+, OH^+, H_2O^+, and H_3O^+, collectively called W^+) in the plume indicated that H_3O^+ was an important component of the Enceladus plume's thermal ionosphere (Cravens et al., 2009), whereas, at energetic, that is, suprathermal energies, O^+ dominates, followed by OH^+ and H_2O^+ (Krimigis et al., 2005). Sergis et al. (2010) found that (a) the contribution of the energetic particles to the total particle pressure becomes significant at >9 R_S and progressively overtakes the thermal plasma beyond 12 R_S, and (b) Saturn's ring current at ~8-18 R_S is intense and variable, being primarily inertial, determined by thermal particles, at <8.5 R_S but increasingly pressure gradient-driven by suprathermal particles in its maximum region (8 to 12 R_S) and certainly farther out.

[2] Charge exchange is especially important for both the ions and the neutral particles in Saturn's inner magnetosphere because of the high neutral gas densities (Mauk et al., 2009). Johnson et al.

(2006) concluded that charge exchange reactions between ions and the neutral particles emitted by Enceladus produce a broad OH cloud and leave a narrow H_2O torus centered on Enceladus’ orbit (a region roughly collocated with a torus of dust and ice grains called the E-ring, see e.g., Showalter et al., 1991; and Cassidy & Johnson, 2010). Although this model reproduced the OH torus observed by HST, it, along with other models that were based on data prior to the Cassini mission (e.g. Richardson et al., 1998; Jurac and Richardson, 2005), had to be revised. Re-analysis of the OH observations by HST revealed that the OH cloud was broader than initially thought (Melin et al., 2009). Additionally, the Cassini Ultraviolet Imaging Spectrograph (UVIS) observed an O cloud twice as broad as the OH cloud (Melin et al., 2009; Persoon et al., 2009; 2013). Further, Cassini observations of the plasma electrons (Schippers et al., 2008) and ions (Wilson et al., 2008; McAndrews et al., 2009; Thomsen et al., 2010; Sittler et al., 2008; Holmberg et al., 2012; 2014; 2017; Livi et al., 2014) greatly improved the understanding of the plasma environment in Saturn’s magnetosphere, so the dissociation and ionization rates of the neutrals had to be revised.

[3] Interactions of the neutral particles in Saturn’s neutral cloud with plasma and solar UV photons, such as charge exchange, electron impact ionization and photoionization, produce O^+, OH^+, H_2O^+, and H_3O^+ (Ip, 1997; 2000; Johnson et al., 2006; Smith et al., 2010; Cassidy & Johnson, 2010; Fleshman et al., 2010a). The combination of these four species is typically called the water group W^+. H_3O^+ is produced largely by charge exchange reactions in the Enceladus torus (Cravens et al., 2009; Fleshman et al., 2010) and was observed to be a prominent W^+ component at thermal energies during Cassini’s Saturn Orbit Insertion (SOI) (Young et al., 2005; Sittler et al., 2008) and during Enceladus flybys (Tokar et al., 2006, 2009; Cravens et al., 2009). However, the overall importance of thermal OH^+ and H_2O^+, and a diminished importance of

thermal H_3O^+, except possibly near Enceladus and at <4.75 R_S, has recently been demonstrated in a preliminary study by Wilson et al. (2015).

[4] Electron impact dissociation and photo-dissociation of H_2O and OH are common sources of H, OH, and O in Saturn's magnetosphere (e.g., Fleshman et al., 2010a,b), efficiently spreading these neutral species throughout the magnetosphere (e.g. Smith et al., 2010a,b). Outside of ~8 R_S, the O cloud predicted by Smith et al. (2010) was not in agreement with the UVIS observations (Melin et al., 2009). Assuming the UVIS results are correct, the discrepancy may be the result of neglecting the effect of neutral-neutral collisions in the model, which is another effective mechanism for spreading neutral particles (Farmer, 2009). Cassidy & Johnson (2010) include the effects of neutral-neutral collisions in their model, and their estimates of the O density are in better agreement with the results from Melin et al. (2009). However, the O density from Cassidy & Johnson (2010) is from a factor of ~2-4 less than that estimated by Melin et al. (2009) at ~10 to 20 R_S. Including the collisions between neutrals significantly increased the H_2O density in Saturn's middle and outer magnetosphere. Models that ignore neutral-neutral collisions (e.g., Johnson et al., 2006) predict a narrow H_2O torus centered on Enceladus with a negligible H_2O density outside of 6 R_S, while including the neutral-neutral collisions results in an H_2O cloud with approximately the same density as OH outside of 7 R_S (Cassidy & Johnson, 2010).

[5] Ion observations from many Cassini orbits revealed that W^+ is the most abundant ion species in Saturn's equatorial plane from thermal (Thomsen et al., 2010) to suprathermal energies (DiFabio et al., 2011). Initial Cassini Plasma Spectrometer (CAPS) observations from SOI indicated that inside of 10 R_S, the thermal water group consists mostly of molecular ions with an

average mass of approximately 18 amu (Figure 16 in Sittler et al., 2008; see also Persoon et al., 2009). Subsequent analysis of CAPS ion data from two Cassini orbits in 2011 by Wilson et al. (2015) found a similar value, ~17.6 amu.

[6] The results from our initial analysis of the Cassini Charge-Energy-Mass Spectrometer (CHEMS) data from two years of Cassini orbits at Saturn was reported by Mauk et al. (2009) in their Table 11.3, where 127-145 keV W^+ was estimated to consist of 46% O^+, 24% OH^+, 25% H_2O^+, and 5% H_3O^+ (see also Difabio, 2012). In the present study, we use the data from CHEMS to separate ~96 keV W^+ into O^+, OH^+, H_2O^+, and H_3O^+. The data are now more clearly understood, the fitting procedure used to determine the composition of W^+ has been refined since the analysis reported in Mauk et al. (2009), and the data interval extended, so the results presented here provide a better estimate of the suprathermal W^+ composition. First, we determine the average W^+ composition in the equatorial ring current region (at L = 7-16 and ±10° Latitude) from 2004-348 to 2010-356, in order to complement DiFabio et al. (2011), the first Cassini study of the long-term variations of the major suprathermal ions in Saturn's magnetospheric equatorial ring current region. Then, extending the radial range to L=21, we present the first examination of suprathermal W^+ and its compositional component variations with L, which we then compare to the thermal ion composition measurements from CAPS reported by Wilson et al. (2015) and model results, including those of Fleshman et al (2013) which provide background in the Wilson et al. analysis.

CHEMS Instrument

[7] CHEMS uses energy per charge (E/Q) selection followed by time-of-flight (TOF) versus energy measurements to identify positive ions with E/Q = 3-220 keV/e. CHEMS has an overall

field of view of 159° x 4° with the large angle divided into three independent 53º sections called telescopes. With the measurement of E/Q, TOF, and kinetic energy with a solid-state detector (SSD) located at the end of the TOF path, the mass, energy and charge state can be determined. The SSD has an electronic threshold of 26 keV. When nuclear defect is included, energy measurements can only be made for protons above 27 keV and oxygen above 47 keV. Herein, we focus on the narrow energy channel at ~96 keV (specifically 95.9 ± 2.9 keV, Vandegriff et al., 2018), which has the lowest W^+ instrumental background, in order to achieve the most effective H_2O^+ and H_3O^+ separation. Below that energy, only the E/Q and mass per charge (M/Q) of an ion are determined. See Krimigis et al. (2004) for a more detailed description of the CHEMS instrument. The entire Cassini/MIMI/CHEMS data set and Cassini ephemeris data are publicly available in the Planetary Data System and can be found at http://pds.nasa.gov.

Method of Data Analysis

[8] We combine the CHEMS data from 78 of the 82 equatorial ring current passes (L = 7-16; Latitude = -10° to 10°) used earlier by Difabio et al. (2011) to study long term variations of the major suprathermal ions at Saturn. We focus our efforts on the main ring current where the highest, most important suprathermal ion fluxes are present (Sergis et al., 2009) in order to separate W^+ into four components: O^+, OH^+, H_2O^+, and H_3O^+. We focus on the ~96 keV/e E/Q channel of telescope 1 data where all four W^+ components are best resolved. Suprathermal ions at Saturn, at the energies considered here, do not rigidly corotate with Saturn outside of ~5-6 R_S (Richardson et al., 1998; Kane et al., 2008), and the observed corotation speeds inside ~6 R_S are < ~50 km/s, small compared to the suprathermal ion speeds. Convection speeds, as estimated in the above studies, are up to ~50-100 km/s lower than rigid corotation speeds in the equatorial ring current out to 15-18 R_S, so only using telescope 1 does not affect our results significantly.

We only use the CHEMS data that includes an energy measurement from the SSD because of its lower background.

[9] A plot of the SSD energy channel, Essd channel, versus the time-of-flight channel, TOF channel, for all 78 ring current passes combined is shown in Figure 1a. Separating the W^+ components was found to be easier using the raw channel values. (DiFabio, 2012), so we do not convert Essd channel and TOF channel to Mass (amu) and M/Q (amu/e). We make an Essd channel cut selecting the data between the horizontal red dashed lines shown in Figure 1a and create a TOF channel histogram of the data (see Figure 1b). All four major components of the W^+ group can be identified, although the H_3O^+ appears as a shoulder. These data are from CHEMS telescope 1 which has the best heavy ion resolution after signal to noise ratio (DiFabio, 2012). We fit these peaks to estimate the abundances of these four species.

[10] We use the ~96 keV O^{++} (E/Q ~ 48 keV/e) TOF distribution from a different energy step (see Vandegriff et al., 2018) as a guide to choosing appropriate fitting parameters for the W^+ species, which overlap. The pre-launch calibration data for ~96 keV O^+ and H_2O^+ are not used because the calibration data distributions tend to be narrower than those in the in flight data due to the mono-energetic and unidirectional nature of the calibration beam. Since the O^{++} ions at E/Q = ~48 keV/e have the same energy as ~96 keV O^+, the ~48 keV/e O^{++} TOF distribution is nearly identical to that of ~96 keV O^+. We can easily fit the ~96 keV O^{++} since there is no overlap from other ion species and use the result in fitting the O^+.

[11] A TOF histogram of the ~96 keV O^{++} distribution for all 78 equatorial ring current passes is shown in Figure 2. The ~96 keV O^{++} distribution is asymmetric, so a simple Gaussian, such as

that used to obtain our preliminary CHEMS data analysis results reported in Mauk et al. (2009), is not the best fitting function. An asymmetric Gaussian fits the central peak of the distribution, where its centroid (the peak's center of symmetry) is at the TOF channel τ_c, which we call the peak's "center". At TOF channels higher than the centroid, the counts decline more slowly than expected for a Gaussian distribution as a result of straggling in the carbon foil (Northcliffe & Schilling, 1970; Gloeckler & Hsieh, 1970), so we must add a small additional term to the Gaussian on the right side of the peak. We refer to this higher-TOF section as the “tail”. The functional form we use to fit the count distribution in TOF channel, τ, is

$$f(\tau) = A\left[e^{-\frac{(\tau-\tau_c)^2}{2\sigma_1^2}} P(-\tau+\tau_c) + \left(e^{-\frac{(\tau-\tau_c)^2}{2\sigma_2^2}} + \frac{(\tau-\tau_c)^2}{100+\left[(\tau-\tau_c)^2\right]^{\alpha}} \right) P(\tau-\tau_c) \right] \quad (1)$$

This function maximizes at the centroid $\tau = \tau_c$ with an amplitude A. The sigmoid function $P(x) = 1/(1+e^{-x})$ is an approximation to the Heaviside function which is ~0 for $x < 0$ and ~1 for $x > 0$. The parameters σ_1 and σ_2 are the Gaussian standard deviations, which we call the "widths", for the $\tau < \tau_c$ and $\tau \geq \tau_c$ sides of the distribution, respectively. The parameter α controls the rate of decline in the tail, in that the function declines as $\sim((\tau-\tau_c)^2)^{(1-\alpha)}$ for $\tau >> \tau_c$.

[12] Gaussian fits performed by von Steiger et al. (2000) on ion species distributions from the Ulysses Solar Wind Composition Spectrometer, a functionally similar type of instrument, showed (in their Plate A2) that the width to center ratios of the TOF distributions vary slowly, so that differences between species spaced closely in TOF channel, such as O^+ and H_3O^+, vary by ≲3-4% percent. Therefore, we use the σ_1/τ_c and σ_2/τ_c ratios as fitting parameters rather than σ_1

and σ_2. The form of our fitting function is similar to the kappa distribution used by Allegrini et al. (2006) to fit the energy distribution of 1-50 keV ions traveling through thin, carbon foils.

[13] Using the Levenberg-Marquardt fitting procedure (Press et al., 1989), we use the function given in Equation 1 to fit the ~96 keV O^{++}. The best fit (reduced $\chi^2 = 0.73$) is obtained with $\alpha = 1.81$ and is shown in Figure 2. Then, when fitting the ~96 keV O^+ distribution, we set its σ_1/τ_c ratio equal to that of the σ_1/τ_c ratio from the ~96 keV O^{++} fit. Because the widths of the molecular ion distributions are not necessarily identical to those of atomic ions, we let the σ_1/τ_c and σ_2/τ_c ratios of OH^+, H_2O^+, and H_3O^+ differ from that of O^+, but force them to be identical for these molecules, because they are dominated by their heaviest atom, O.

[14] Although the CHEMS pre-launch calibration data show that the W^+ tail counts grow with increasing M/Q, we were unable to determine how much the α parameter would vary among the four species from the in-flight data. Thus, we assumed that the α parameter is same for all four species. This assumption increases the uncertainty in our estimates of the ion abundances, particularly that of H_3O^+. In order to determine the sensitivity of our results to the form of the fitting function, we performed three different types of fits on the W^+ distribution with these conditions on α: type 1: asymmetric Gaussian ($\alpha = \infty$), type 2: requiring α to equal the value from the O^{++} fit ($\alpha = 1.81$), and, type 3: allowing α to vary. (We include this discussion although, in the results of our analysis, variations of the distributions' tails tended to be of minor importance.) For the first two types, we require the σ_2/τ_c value for O^+ to equal the results from the O^{++} fits. Since the value of the α parameter affects the value of σ_2, we let the O^+ σ_2/τ_c and α vary for the third fit. The centers τ_c for all four species and the σ_1/τ_c ratio for the molecular ions

are only allowed to vary in the asymmetric Gaussian fit (type 1). In the type 2 and 3 fits, the centers and molecular ion σ_1/τ_c ratio are forced to equal the values from the type 1 fit. We let the amplitudes A and σ_2/τ_c ratio of the molecular ions vary for all three types of fits.

[15] Figure 3 shows our best fit (reduced χ^2= 4.0) of the entire W^+ distribution, which is found using the type 3 fit and with α=1.90. Numerically integrating each peak from the type 3 fit provides our best estimate of the O^+, OH^+, H_2O^+, and H_3O^+ counts. We then convert the counts into partial number density and calculate the fractional abundance relative to W^+. As discussed in the next section, the type 1 and 2 fits are used to determine the upper and lower limits of the H_3O^+ abundance.

[16] After obtaining the fits in the main ring current (L = 7-16; Latitude = -10° to 10°), we divide the Cassini passes by L shell and look for variations with L in the L = 7-21 range. When fitting the data by L shell, the statistics are worse, and we only let the amplitudes of the peaks vary, forcing the center τ_c, σ_1, σ_2, and α of each species peak to be the same as the results from the L = 7-16 fit. We use a ΔL = 1 for L = 7 to 11 where there are sufficient counts, but we must combine L shells beyond this distance where the counting statistics decline, using ΔL = 2 for L = 11 to 15, and ΔL = 3 for L = 15 to 21.

Results and Discussion

[17] <u>Results and comparison with earlier studies</u>. Table 1 lists the counts from the best fit to the W^+ distribution plotted in Figure 3 (i.e., the type 3 fit with α = 1.90) along with the partial number densities and the relative abundances of the ~96 keV W^+. The W^+ group has an average mass of 16.7 amu and consists of ~53% O^+, ~22% OH^+, ~22% H_2O^+, and ~3% H_3O^+. Since the

number of counts in the distribution tails contain only a small percentage of the total counts, our estimates of the O^+, OH^+, and H_2O^+ abundances do not vary significantly among the three types of fits. The quoted uncertainties for these three species reflect the statistical uncertainties from our type 3 fits. Because H_3O^+ is much less abundant and the tails from the other three species make up a significant fraction of the counts at the location of the H_3O^+ peak, our estimate of the H_3O^+ counts strongly depends on the α parameter. This can possibly introduce a larger systematic error and the quoted H_3O^+ uncertainties reflect the range of values from our three different fits. The asymmetric Gaussian fit with no tail provides an upper limit on the H_3O^+ abundance, while forcing $\alpha = 1.81$, which overestimates the tail counts, provides a lower limit on the H_3O^+ abundance.

[18] The partial number densities and fractional abundances of the four ~96 keV W^+ components are plotted versus L in Figures 4a and 4b, respectively. Figure 4a shows that all four W^+ components increase similarly at L ~ 8-10, peak at L ~ 9.5, and decrease at L < ~9, but not quite similarly. Figure 4b shows that (a) fractional O^+, OH^+, and H_2O^+ vary little from L = 5-21, with each species' variations being statistically insignificant, (b) fractional H_3O^+ is approximately constant at L > ~13, and (c) the enhancement of fractional H_3O^+ probably starts at L ~ 13, but certainly only increases monotonically inside of L ~ 11, increasing by almost a factor of ~3 above fractional H_3O^+ levels at L > ~13. Paranicas et al. (2008) noted that ~5-100 keV H^+ and O^+ (products of the magnetospheric processes CRAND and , respectively) populate Saturn's inner magnetosphere episodically, being energized by injections, and concluded that they are then primarily lost to charge exchange in the Enceladus torus as they drift inward. We agree that this interpretation is consistent with our W^+ radial variations in Figure 4a. The W^+ components may originate from any object in Saturn's magnetosphere before their dispersal and subsequent

inward transport from L ~ 15-20, but most are currently presumed to originate in Saturn's main rings and the Enceladus neutral torus. On their way inward, the ions' partial number density at a given energy increases, peaking at L ~ 8-10, inward of which losses increase as they encounter the neutral torus. Paranicas et al. (2008) demonstrated that energetic/suprathermal O^+ flux decreases persistently in to L ~ 5.5-6.5 (depending on magnetospheric conditions), where it then becomes undetectable (see Figure S3 in the Supporting Information). They note that "...The shape of the flux drop off inward to the planet has different behavior on each orbit we have surveyed and is not related to the locations of the moons." They argued that the W^+ components are transformed by the neutral gas cloud in this region which converts the inward drifting ions to energetic neutral atoms via charge exchange. Kollmann et al. (2011) show that ~46 keV H^+ and ~91 keV e^- display differential intensity peaks at ~9 < L < ~10.5 and L ~ 8, respectively (see Figure S4 in the Supporting Information), similar to the energetic protons and oxygen in Paranicas et al., with fluxes decreasing in to L ~ 5-6. Christon et al. (2014) show that 83-167 keV W^+, a portion of its straggling tail W^+_{tail} at ~22–26 amu/e, O_2^+, and $^{28}M^+$ all display peaks at L ~ 9 and decreases in to L ~ 6 (see Figure S5 in the Supporting Information). The fractional W^+_{tail} varies little outside of L ~ 7, similar to this study's fractional O^+, OH^+, and H_2O^+, and like the fractional H_3O^+ component, the fractional O_2^+ and $^{28}M^+$ abundances vary insignificantly at L ≥ 13, but vary inside L ~ 13. However, rather than increasing as fractional H_3O^+ does, fractional O_2^+ and $^{28}M^+$ levels decrease markedly inside L ~ 13, much further than the fractional H_3O^+. Note though, in this study, while the variation is not statistically significant, fractional H_3O^+ is disrupted with respect to its behavior beyond L ~15 and starts increasing inside L = 13. Interestingly, the magnetic pressure of Saturn's inner, "core", dipolar magnetic field is rather well ordered out to ~10 R_S, with disturbed ordering persisting somewhat out to ~13 Rs, beyond which low level disturbed magnetic pressure extends to larger radial distances (Sergis et al., 2010), suggesting that the L < 10 region may be characteristically differentiated from the L > 13 magnetosphere. It is apparent that the H_3O^+ is not depleted as much as the other three W^+ components inside of L ~ 10, suggesting some as yet unidentified, differentiated interaction(s) possibly resulting from this magnetospheric magnetic field transition near L ~ 10 occur near the neutral torus for these ions.

[19] The energetic O^+, OH^+, and H_2O^+ fractional abundances in Figure 4b show no significant variation with L from 7 to 21; they do not deviate far from their average values throughout the main ring current. The dashed box encompasses the entire radial and abundance range of the four thermal ion fractional abundances from Wilson et al. (2012). Suffice it to say, most of the thermal ion radial variation is evident at L < 8. Clear depiction of both data sets, not necessary here, is presented in Figure S2 in the Supporting Information. We expect few, if any, correlated variations or processes between the energetic and thermal-W^+-components as the thermal W^+ components propagate outward from their inner magnetospheric source region, and the suprathermal W^+ components diffuse inward from their outer magnetospheric acceleration region(s). The suprathermal W^+ components have much wider variation than the thermal components, with O^+ being somewhat more abundant and H_3O^+ being much less abundant than either OH^+ or H_2O^+.

[20] The suprathermal H_3O^+ fractional abundance has an average value of ~0.017 at 13 < L < 21 and shows no measurable radial dependence. However, at L < 10, the H_3O^+ partial density peak and relative decrease are not as substantial as that of the other W^+ components, resulting in its fractional abundance increasing to H_3O^+/W^+ ~0.048 - apparently due to a weaker interaction with the nearer-Saturn environment. One possible cause of this more moderate decrease of H_3O^+ at

lower L might be that the H_3O^+ charge exchange lifetime is longer than those of O^+, OH^+, and H_2O^+, or, alternatively, that H_3O^+ interactions with the negatively charged E-ring grains inside the orbit of Rhea (~8.74 Rs) are weaker than those of O^+, OH^+, or H_2O^+. The fractional abundances of suprathermal ions with longer charge exchange lifetimes (smaller cross sections), such as possibly H_3O^+, would be expected to increase with respect to other ions whose cross sections are larger, as losses become more important going inward. Unfortunately, although cross sections for 10's of eV-energy W^+ ions are available (e.g., Lishawa et al., 1990), to our knowledge, the cross sections for ~10-500 keV water group ions colliding with Saturn's most important thermal neutral cloud atoms and molecules (O, OH, and H_2O) are not all available in the literature. As a result, we can only offer qualitative analysis of the W^+ component charge exchange lifetimes below using available lower energy charge exchange cross sections as a guide. An alternative, independent, and concurrent process contributing to the difference of the H_3O^+ radial dependence might result from varying strengths of interactions between H_3O^+ and the other W^+ components with the charged E-ring grains. E-ring grains are observed to vary in size, from several nanometers up to tens of micrometers and have radially varying charged components, in which negatively charged grains dominate inside the orbit of Rhea, transitioning to both positive and negative within an Rs or so around the orbit of Rhea, and then become preponderantly positive with increasing distance from Saturn outside the orbit of Rhea, as reported, for example, by Wahlund et al. (2005), Sittler et al. (2006), Kempf et al. (2008), Hsu et al. (2013), and Ye et al. (2017). We address both possible scenarios below.

[21] In Figure 4b we compare our fractional W^+ abundance results at ~96 keV to the range of the preliminary results for the thermal plasma fractional abundances reported by Wilson et al. (2015) in their Figure 3. Both studies analyze near-equatorial data, with a radial overlap at L = 7-10; that

is, this study uses L = 7-21 and Wilson et al. (2015) used R_S = 4.75-10. Considering the small 7 ≤ L ≤ 10 overlap region, the fractional abundance values are somewhat comparable, although the range of fractional suprathermal ion abundances is much greater than that of the thermal ions. Ratio ranges from the two studies and model results from Figures 3 in Fleshman et al. (2013) and Wilson et al. (2015) are listed in Table 2. To date, we are unaware of any models characterizing the energetic/suprathermal water products' distribution, propagation, and/or interactions in Saturn's magnetosphere. The observed OH^+ and H_2O^+ fractional abundances are roughly comparable in the two energy ranges, although the thermal population values are somewhat larger. Major differences between the thermal and energetic population O^+ and H_3O^+ fractional abundances are evident: the O^+ fractional abundance is much larger for the suprathermal ions and the H_3O^+ fractional abundance is much smaller for the suprathermal ions. The thermal ion fractional abundances are all between ~0.18 and ~0.30, which is about twice the range of the H_2O^+ and OH^+ suprathermal uncertainties. Understanding that acceleration to suprathermal energies is not instantaneous, one might expect for extensive dissociation of the W^+ molecular species to occur, producing relatively more atomic O^+. In summation, the suprathermal fractional abundances show little radial variation except for the H_3O^+ increase by a factor of ~3 from L ~ 13 to L ~ 7. Of note, the thermal H_3O^+ fractional abundance also shows a large increase with decreasing L. However, at thermal energies, the fractional abundances of the other species also show radial variations over the L = 7-10 range with the O^+ and OH^+ increasing and the H_2O^+ decreasing with increasing L.

[22] <u>Origin of the suprathermal ions</u>. The majority of Saturn's water group ions are produced by the dissociation and ionization of the neutral H_2O emitted from the Enceladus plumes (Burger et al., 2007; Smith et al., 2010; Cassidy & Johnson, 2010). Since the ions observed here are much

more energetic than the thermal ions, we must consider the acceleration and transport processes when comparing our results to the thermal ion observations and neutral cloud models. The most likely acceleration processes are injections (Mauk et al., 2005; Hill et al., 2005; Burch et al., 2005; Paranicas et al., 2007; Rymer et al., 2009) and inward radial diffusion (Van Allen et al., 1980; Armstrong et al., 1983) conserving the first and second adiabatic invariants. Injection events are a result of the centrifugal interchange instability where narrow "fingers" of hot plasma are injected inward and replace broad, outward flowing cold plasma. Injection events can be grouped into two categories: low energy and high energy (Mitchell, Carbary, et al., 2009). Low energy events originate at L = 9-11 (Rymer et al., 2009), while high energy events originate in the magnetotail (Mitchell, Krimigis, et al., 2009). Acceleration by inward radial diffusion also requires the thermal ions to start in the outer magnetosphere, so the accelerated ions studied here likely reflect the plasma ion composition in the outer magnetosphere, a region not addressed by Wilson et al. (2015).

[23] The composition of the thermal ions in the outer magnetosphere depends on a number of factors. One is the ionization rate of the neutral particles in the outer magnetosphere. Although possible differences among the neutral species' ionization and dissociation rates prevent us from directly comparing the ion composition to the neutral densities, our results do provide constraints. If a large percentage of the thermal ions in the outer magnetosphere is produced by the ionization of neutrals in this region, then the suprathermal ion composition will closely reflect the neutral particles that were initially ionized in the outer magnetosphere.

[24] Because the ionization rates are much higher in the inner magnetosphere, we must consider the possibility that thermal ions produced in the inner magnetosphere are then transported to the

outer magnetosphere where they are accelerated. As discussed above, broad outward flows of cold plasma are consistent with the properties of the centrifugal interchange instability (Hill et al., 2005; Rymer et al., 2008). Electron and ion observations suggest that this outward transport process is not adiabatic and does not cool the plasma (Rymer et al., 2007, 2008; Wilson et al., 2008). Therefore, the outward transport of thermal ions followed by acceleration in the outer magnetosphere can produce ions at suprathermal energies. Observations by Cassini UVIS (Melin et al., 2009) and models of the neutral cloud (Smith et al., 2010; Cassidy & Johnson 2010) indicate that the neutral O cloud is much broader than the neutral OH and H_2O clouds. Outside of 6 R_S, the neutral O density is larger than that of OH and H_2O, and the neutral O density is about an order of magnitude greater than the other water group neutrals near ~20 R_S (Cassidy & Johnson, 2010), whereas, near the orbit of Rhea, ~8.75 R_S, the neutral O to OH (and, likely H_2O) density ratio is modeled to be from ~2 to ~3.5 (by Smith et al., 2010 and Cassidy & Johnson, 2010, respectively). Since the ionization rates of the neutral particles throughout the magnetosphere are estimated to be approximately the same (Cassidy & Johnson, 2010), we would have expected the suprathermal O^+/OH^+ and O^+/H_2O^+ ratios to be larger than our observed value of ~2.4, because their presumed source is closer to ~20 R_S than ~8.75 R_S.

[25] It is possible that a large percentage of the ions in the outer magnetosphere is produced inside of 10 R_S, where the difference between densities of neutral O and of neutral molecules is not as large, as noted above, and the ions are then transported to the outer magnetosphere. However, Wilson et al. (2015) find that O^+ is generally the least abundant water-group ion at thermal energies, not the most abundant water-group ion, as at suprathermal energies. Wilson et al. (2015) reported that the mean mass of thermal water group ions has a mean of 17.56 amu in the radial region of 4.75 to 10 R_S, and decreases with distance from Saturn. On the other hand,

the mean mass of suprathermal ions, 16.7 amu, reflects the large percentage of suprathermal energy O^+, ~2.5 times greater than OH^+ or H_2O^+ throughout $7 \leq L \leq 16$. Because of the larger fractional abundance of molecular ions inside of 10 R_S, the outward transport of these ions would result in a lower O^+/W^+ ratio relative to the neutral O/W ratio. To perform quantitative analysis, better constraints on the ion transport rates, production rates, and loss rates are needed. However, our observation that W^+ consists mostly of O^+ is qualitatively consistent with the broad atomic O cloud observed by Cassini UVIS (Melin et al., 2009) and predicted by some models (Smith et al., 2010; Cassidy & Johnson, 2010; Dialynas et al., 2013). Our observation of nearly equal amounts of suprathermal OH^+ and H_2O^+ suggests that neutral H_2O is spread to Saturn's middle or outer magnetosphere rather than confined to a narrow (~2-3 R_S) torus centered on Enceladus' orbit. This result supports the conclusions of the Cassidy & Johnson (2010) model, which predicts approximately equal neutral OH and H_2O densities spread outside of 7 R_S. If neutral H_2O were confined to a narrow torus near 4 R_S as suggested by other models (e.g. Johnson et al., 2006; Smith et al., 2010), we would expect very low abundances of suprathermal H_2O^+ compared to O^+ and OH^+.

[26] Our results do not rule out the possibility that most of the H_2O^+ is produced near Enceladus' orbit and then transported to the outer magnetosphere where it is then accelerated. However, this scenario seems unlikely, because we would expect the suprathermal H_2O^+ fractional abundance to be similar to that of the suprathermal H_3O^+. Thermal H_3O^+ is the most abundant ion species in the Enceladus torus where the majority of it is produced via charge exchange reactions (Sittler et al., 2008; Cravens et al., 2009; Fleshman et al., 2010a). As the H_3O^+ is transported outward, its fractional abundance drops significantly due to its short recombination lifetime in the Enceladus torus (Ip, 2000; Sittler et al., 2008). Because the recombination lifetime of H_2O^+ is even shorter

than the H_3O^+ lifetime in the Enceladus torus (Fleshman et al., 2010b), we would expect a similar decrease in the thermal H_2O^+ fractional abundance. Therefore, the production of H_2O^+ in the inner magnetosphere followed by outward transport and acceleration in the outer magnetosphere would probably not result in our observed suprathermal H_2O^+/H_3O^+ ratio of ~7.8. A more detailed model is necessary before this possibility can be conclusively ruled out.

[27] L dependence at L < ~9. We now qualitatively discuss the processes that might cause the large losses of suprathermal ions inside of L ~ 9. This is a qualitative discussion because, to our knowledge, relevant functional forms and/or laboratory measurements for the water group suprathermal ions of interest relevant to their interactions with the thermal ions and neutral particles present in the E-ring (or Enceladus torus) and discussed herein do not exist or are not available in the literature. In this discussion, we will also present some measurements at low center of mass, CM, collision speeds because, they are all that exists. Charge exchange and proton-transfer cross sections likely vary among the species studied herein and are probably responsible for most of the observed changes/differences in the relative abundances of the W^+ constituents. For W^+ constituents, fractional differences appear to be seen only for H_3O^+, but note that important differences with respect to W^+ exist for heavier important molecules at Saturn (see Figure S5 in the supporting information).

[28] Charge exchange with neutral gas. Consider the charge exchange reaction involving an ion A^+ colliding with the neutral B ($A^+ + B \rightarrow A + B^+ + \Delta E$), where ΔE is the difference between the ionization energies of A and B. For resonant processes (i.e. $\Delta E = 0$), the charge exchange cross section decreases with energy and behaves like $\sigma = (C\text{-}D*\ln(v))^2$, where C and D are constants and v is the relative velocity (Dalgarno, 1958). At low velocities, cross-sections of non-resonant

collisions are smaller than those of resonant collisions and increase with increasing velocity (Rapp and Francis, 1962). Non-resonant cross sections maximize at a velocity, v_{max}, that can be approximated by the Massey adiabatic hypothesis (Massey, 1949):

$$v_{max} = \frac{v_o \left|\Delta E\right|}{h} \tag{2}$$

where $v_o = 7\text{x}10^{-8}$ cm and h is Planck's constant. Above this maximum velocity, the non-resonant cross section converges with the cross section of the resonant collision. The collision cross section maximizes at higher velocities as the difference in ionization energies increase.

[29] Although the above relation is only meant for slower collisions, in the absence of related laboratory results and in order to get a sense of any differences that may exist between H_3O^+ and the other W^+ components, we apply Equation 2 to collisions of the water group ions with atomic O, which is ~6 times more plentiful than OH at ~10 R_S as shown by Melin et al. (2009). The ionization energies of O, OH, and H_2O are 13.6 eV, 13.0 eV, and 12.6 eV (Weast, 1968; Wiedmann et al., 1992), respectively, while the ionization energy of H_3O is much less at 5.5 eV (Melin et al., 2005). Using these ionization energies, the collision cross sections of OH^+ on O and H_2O^+ on O are estimated to peak at $v_{max} \sim 1\text{-}2\text{x}10^7$ cm/s, while the H_3O^+ on O cross section is estimated to peak near at $v_{max} \sim 1.4\text{x}10^8$ cm/s, an order of magnitude larger. Because the velocities of ~96 keV OH^+ and H_2O^+ are much greater than the velocity at which the cross section maximizes, we might expect the charge exchange cross sections of these species to be approximately the same. The cross section of ~96 keV H_3O^+, however, will not have reached its maximum value and will be less than the cross sections of the other three ion species. Therefore, ~96 keV H_3O^+ will have a longer lifetime than the other ~96 keV water group ion species. As a result, the fractional abundance of H_3O^+ should be expected to increase inward, while the fractional abundance of O^+, OH^+, and H_2O^+ would not show significant variations. The result of

this argument is qualitatively consistent with and provides a reasonable framework for understanding why suprathermal H_3O^+/W^+ increases with decreasing L, and has a very different explanation than that for thermal H_3O^+/W^+ increasing with decreasing L. Hopefully, in future analysis related to these particles in this process, the charge exchange cross sections of these energetic ions will be more fully documented and other reactions, such as dissociation and interactions with charged dust should also be included and modeled for these suprathermal ions in Saturn's magnetosphere.

[30] Grain interactions. Grains and dust permeate Saturns magnetosphere, as demonstrated in Figure 5, where we show three distributions of 0.1-3.0 μ grains that Hornáyi et al. (2008) modeled from a continuous scan of grain densities derived from data measured during Cassini's ring-plane crossing on Orbit 7. Their study provides one of the few snapshots of the magnetosphere's grain population. Three different size ranges demonstrate the spatial distribution of grains relative to our overlaid W^+ measurements in the upper panels. A large measurable portion of E-ring grains have either positive or negative charge (e.g., Kempf et al., 2006; Ye et al., 2014). Kempf et al. (2006) found that grains bigger than 2–3 μm detected inside Rhea's orbit (L ~ 8.75) were always negatively charged, whereas grains outside Rhea's orbit were all positively charge. Dong et al. (2015) determined that the size distribution of nanometer-sized grains obtained by CAPS (~0.001 μm, herein called dust) suggests that ~1-10 nm sized grains dominate both charge density and number density, at least near Enceladus. Little information is available on total grain population characteristics (from nanometer to micrometer sizes) and their properties throughout Saturn's magnetosphere, except near Enceladus' orbit. Nevertheless, we estimate below whether ion interactions with Saturn's charged grain/dust environment should be considered in addition to Saturn's neutral gas populations, even when exclusion of the grains

might provide acceptable explanations of phenomena in Saturn's magnetosphere without such consideration. The grain interactions we consider here are a possible alternative reason for the difference between the radial profiles of H_3O^+ and the other W^+ components.

[31] The water-group ions should be attracted to any negatively charged particles, grains or ions, in the dusty plasma through electrostatic attraction, and repulsed by positively charged particles. The W^+ components' electric dipole moments (∂) for OH^+, H_2O^+, and H_3O^+ have different values: 2.32, 2.40, and 1.44 D (debye), respectively (see e.g., González-Alfonso et al., 1983; Vogelius et al., 2004; and Botschwina et al., 1983). For comparison, neutral molecules can have an induced electric dipole moment, two are (up to) ∂_{OH} = 1.65 D for OH, Werner et al., 1985, and ∂_{H2O} = 1.85 D for H_2O, Dyke & Muenter, 1973), so the H_3O^+ dipole moment is ~40% smaller than those of OH^+ and H_2O^+ and comparable to induced neutral molecule dipole moments. Given that, H_3O^+ will be less attracted to the prevalent negatively charged E-ring grains near and inside of Rhea's orbit than the other W^+ components. H_3O^+ would therefore have a longer mean free path in the E-ring planetward of Rhea, if not for some distance outside of L ~ 9. Some portion of the negatively charged E-ring grains will capture W^+ components, more likely the O^+, OH^+, and H_2O^+ than the H_3O^+. This weakness of the H_3O^+ dipole moment is a possible, as yet unexplored, interaction difference with the E-ring material, in addition to the aforementioned possible cross section difference between H_3O^+ and the other W^+ components. The difference in dipole moments would result in fewer collisions with and less attraction between charged grains and H_3O^+ than with the other W^+ components.

[32] E-ring grain measurements in two different size ranges by Cassini instruments were: (a) ≥9 µm by design, Cosmic Dust Analyzer, CDA (Srama et al., 2004; 2011; Kempf et al., 2008; and

>0.5 by impact identification algorithm, Kempf et al., 2004); (b) ~2-10 μm from spacecraft charging, Radio Wave and Plasma Wave Science (RPWS) investigation (Gurnett et al., 2004; Ye et al., 2014; 2016); and (c) ~0.6-3 nm by CAPS, from large energy-per-charge measurements (e.g., Hill et al., 2012; Dong et al., 2015). Only CDA was designed to measure the grains and dust, but the measurements have been compared and appear to be complementary (Meier et al., 2014; Dong et al., 2015). Complementary overlays of data from Kempf et al. (2006) and Ye et al. (2014) in the bottom panel of Figure 5 show that grains >0.5 microns detected inside Rhea's orbit, ~8.75 Rs, are mostly negatively charged and grains outside Rhea's orbit were positively charged, with the typical potentials being about -2 V and +3 V, respectively (Figure 1 of Kempf et al., 2006). However, the Ye et al. (2014) data clearly show that some negatively charged grains persist beyond Rhea's orbit. Dust, detected in and near the Enceladus plume with both negative and positive net charges (Hill et al., 2012), likely follows a similar, but more likely complex large scale pattern, than the grains (e.g., Engelhardt et al., 2015), but, to our knowledge, this has not yet been fully investigated. In the Appendix, we estimate the ratio of mean free paths for H_2O^+ near the orbits Enceladus and Rhea (a) in O and OH gas from the models of Cassidy and Johnson (2010), and (b) in 1 and 2 nm dust at expected densities there, using dust (CAPS) and grain (CDA and RPWS) measurements at Enceladus' orbit and values at Rhea's orbit, using CDA's measured radial grain variation and complementary CDA and RPWS data near Rhea's orbit combined with extrapolated dust estimates assuming the same radial variation as grains. The range of estimates for the ratios of H_2O^+ mean free paths in neutral O and OH gas to H_2O^+ mean free paths in uncharged grains and dust are neither orders of magnitude apart nor widely divergent from unity, ≈1, where the mean free path estimates are equal; the estimates range instead from ratios of ~2 to ~0.2, for dust sizes at 1 and 2 nm, respectively, values slightly below and slightly above those characteristic of the most likely nanograin size (Dong et al., 2015).

Therefore, depending on the true gas and grain densities and grain sizes in the E-ring near the orbit of Rhea, in addition to charge exchange interactions, consideration of ion-grain/dust interactions through focused modeling, might be necessary in order to fully understand the radial variations of suprathermal W^+ component partial densities.

Concluding Remarks

[33] The fractional abundances of suprathermal OH^+ and H_2O^+ are comparable and both consistently near ≈0.2 for $7 < L < 21$, compared to (a) thermal OH^+ clearly increasing from ~0.23 to ~0.3 and and (b) thermal H_2O^+ decreasing somewhat from ~0.31 to ~0.26 from 5 to 10 R_S. Over $7 < L < 21$, the fractional abundance of suprathermal O^+ is much larger than the other W^+ components and the fractional abundance of suprathermal H_3O^+ is much smaller than the other W^+ components. Suprathermal O^+ (H_3O^+) fractional abundance is larger (much smaller) than thermal O^+ (H_3O^+) fractional abundance in the ~7-10 R_S radial range. The suprathermal O^+, OH^+, and H_2O^+ fractional abundances show no significant variation with L over the range L = 7-21. The suprathermal H_3O^+ fractional abundance, with an average value of 0.017, shows no dependence on L at L = 13-21. Inside of L = 13, however, the suprathermal H_3O^+ fractional abundance increases substantially to 0.048 at L = 7-8, a factor of 2.8. The radial variations of suprathermal W^+ components are distinctly different from available thermal energy W^+ components radial variations. A full examination of the interesting H_3O^+ variation inside L ~ 9 is hampered by both the lack of charge exchange cross sections for suprathermal water-group ions on thermal O and H_2O and the lack of more comprehensive information.

Appendix 1. Scattering of a water ion in the near-Rhea E-ring

In simple grazing, elastic collisions, the mean free path of an ion traveling in a neutral gas (or grain field) of interaction distances d is determined, in part, by the ratio of the distance traveled (vt) to the product of the interaction volume (□d^2 vt) times the number of target particles per unit volume (Nt).

We assume that:

(a) H_2O^+ is the representative ion for the water group;

(b) O or OH are the most likely neutral gas targets (Cassidy & Johnson, 2010) with ion radius, r_N, and density N_N;

(c) The incoming ion (I) and a target (T) neutral particle will interact if they touch, that is, if the distance between their centers is $d \le (r_I + r_T)$. The interaction area, or cross section, is $\pi(r_I + r_T)^2$; and (d) In estimating the varying scenarios, the grain population is characterized by their minimum grain radius, r_G, with $r_G >> r_N$, and density N_G.

A general form of the MFP, given in Chemistry LibreTexts. 4.12: The Frequency of Collisions between Unlike Gas Molecules (https://chem.libretexts.org, 2019), is:

MFP = $vt \;/\; (\pi(r_I + r_T)^2\, vt\, N_T)$, where,

v = speed of the ion through the medium,

t = time for the ion to travel the distance vt,

r_I = the radius of the ion,

r_T = the radius of the target population's particles, r_T, which, for the neutral gas are $r_{N,O}$, for O atoms, or $r_{N,H2O}$, for H_2O molecules, the most populous E-ring neutrals (see the reference list below), and the second case, E- ring grains, characterized above, and

N_T = the target particle population's density (the same subscripts apply).

For our purpose of obtaining order of magnitude estimates for ions in different media, we simply need to examine $\Gamma_{N:G}$, the ratio of the ions' mean free paths in the neutral gas (N) to grain (G) populations, which reduces to:

$$\Gamma_{N:G} = \frac{MFP_N}{MFP_G} = \frac{vt \;/\; (\pi(r_{I+}r_N)^2 \, vt \, N_N)}{vt \;/\; (\pi(r_{I+}r_G)^2 \, vt \, N_G)} \sim \frac{(r_{I+}r_G)^2 \, N_G}{(r_{I+}r_N)^2 \, N_N} \qquad \text{(A1).}$$

If $\Gamma_{N:G} \approx 1$, the ion's MFP in the neutral gas is about the same as it is in the grains. It is easier for the ion to pass through (a) the neutral gas if $\Gamma_{N:G}$ is >> 1, or, vice versa, (b) the grains if $\Gamma_{N:G}$ is << 1. We calculate values for a range of estimated situations below, as detailed information for the grains throughout Saturn's magnetosphere is not complete in order to see if the grains should even be considered as possibly affecting the suprathermal ion populations.

Neutral Gas. For the neutral gas, we use the models of Cassidy & Johnson (2010) and Smith et al. (2010), which is accepted as being a reasonable representation of the neutral gas populations in Saturn's magnetosphere derived from Cassini measurements. Their model shows that while the O and OH number densities, N_O and N_{OH}, respectively, are nearly equal (to within ~25%) at Enceladus' orbit, N_O is ~3.5 times higher than N_{OH} at Rhea's orbit. As they are the two most populous neutral species, we perform calculations for both O and OH, because, OH, with ~22% of the plasma density near Rhea, can still produce measurable effects in that region.

Grains and Dust. Saturn's magnetosphere is filled with an icy, dusty plasma, and is the closest environment to Earth similar in any way to vast expanses of the interstellar medium. The radial variation of CDA data collected from 2004-200 to 2008-259 for nanometer grains and the fit to it in Figure 11 of Srama et al. (2011) is a clear, comprehensive, long-term display of magnetospheric-scale E-ring grain data. Srama et al. (2011) do not state whether data within several to tens of Enceladus radii, near the moon and its plume, were included in this long-term data set or not, but the display, a data collection intended to represent an overall average perspective of the E-ring grains, suggests that near-Enceladus data were not included. To our knowledge, no study E-ring data at/near the orbit of Enceladus, characterizes the azimuthal variation of the grain population in a manner useful in our study. In their Figure 11, Srama et al. (2011) fit the radial variation of CDA densities with a power law, given as $n(r) = 20 (r - 2.8)^{-4.6}$, in the range ~4.5-19 R_S, for data obtained from 3 to 19 R_S. The n(r) fit is very close to the density averages plotted from ~5 to ~15 R_S at intervals of 1-3 R_S. The mean density point plotted at <5 R_S is far below their n(r) fit, consistent with their statement that, on account of dead time limitations, the CDA counting rates saturated at times near Enceladus' orbit, 3.95 R_S, so that the derived number density from those saturated counting rates (as shown) at < ~4.5 R_S are a lower limit. The fall-off with increasing radial distance is similar to other reports (see e.g., Ye et al., 2016), so we take their fit in this radial range as a reliable representation of average-Enceladus orbit data which does not include the near-moon plume flux and, therefore, representative of the overall average E-ring population from ~3.95 - 15 R_S at locations not directly influenced by the Enceladus plume. Therefore, for our purposes, we can estimate the average grain density near the orbit of Rhea, 8.75 R_S, from their n(r) fit in determining $\Gamma_{N:G}$ near Rhea's orbit from measurements typically made near the orbit of Enceladus. Their measurements are for micrometer sized grains, whereas most of the grains are at nanometer sizes, at least near Enceladus. The values of $\Gamma_{N:G}$ we obtain (see Tables S1-S3 in the Supporting Information) range within a factor of ~3-4 about 1 for characteristic grain sizes of 1 and 2 nm. This is not an exhaustive assessment and only elastic collisions were considered, as well as much of the necessary, relevant information particular to the grains and the gas is not yet well established, nor will be ion the near future. Nevertheless, these estimates are not orders of magnitude higher or lower than unity, they are clustered around ~1, the value at which the H_2O^+ mean free path in the dust/grain populations is approximately equal to that in the neutral gas populations. Finally, this exercise does suggest that, when the extant grain population sizes and gas and grain densities in Saturn's magnetosphere are known: that is, measured, confirmed, and characterized, the effect of grains on Saturn's suprathermal ions and various other observables can be established and might be found to be of significance.

References

Allegrini, F., McComas, D. J., Young, D T., Berthelier, J. -J., Covinhes, J., Illiano, J. -M., et al. (2006). Energy loss of 1-50 keV H, He, C, N, O, Ne, and Ar ions transmitted through thin carbon foils. Reviews of Scientific Instruments, 77(4). https://doi.org/10.1063/1.2185490

Armstrong, T. P., Paonessa, M. T., Bell II, E. V., & Krimigis, S. M. (1983). Voyager observations of Saturnian ion and electron phase space densities. *Journal of Geophysical Research, 88*, 8893-8904. https://doi.org/10.1029/JA088iA11p08893

Botschwina, P., Rosmus, P., & Reinsch, E. A. (1983). Spectroscopic properties of the hydroxonium ion calculated from scep cepa wave functions. *Chemical Physics Letters, 102*, 299-306. https://doi.org/10.1016/0009-2614(83)87045-6

Branscomb, L. M., (1966). Photodetachment cross section, electron affinity, and structure of the negative hydroxyl ion. *Physical Review, 148*, 1, 11-18. https://org/doi/10.1103/PhysRev.148.11

Burch, J. L., Goldstein, J., Hill, T. W., Young, D. T., Crary, F. J., Coates, A. J., et al. (2005). Properties of local plasma injections in Saturn's magnetosphere. *Geophysical Research Letters, 32*, L14S02. https://doi.org/10.1029/2005GL022611

Burger, M. H., Sittler Jr., E. C., Johnson, R,. E., Smith, H. T., Tucker, O. J., & Shematovich, V. I. (2007). Understanding the escape of water from Enceladus. *Journal of Geophysical Research, 112*, A06219. https://doi.org/10.1029/2006JA012086

Cassidy, T. A., & Johnson, R. E. (2010). Collisional spreading of Enceladus' neutral cloud. *Icarus, 209*, 696-703. https://doi.org/10.1016/j.icarus.2010.04.010

Christon, S. P., Hamilton, D. C., Mitchell, D. G., DiFabio, R. D., & Krimigis, S. M. (2014). Suprathermal magnetospheric minor ions heavier than water at Saturn: Discovery of $^{28}M^+$ seasonal variations. *Journal of Geophysical Research, 119, 7*, pp. 5662-5673.

https://doi.org/10.1002/2014JA020010

Cravens, T. E., McNutt Jr., R. L., Waite Jr., J. H., Robertson, I. P., Luhmann, J. G., Kasprzak, W., & Ip, W. -H. (2009). Plume ionosphere of Enceladus as seen by Cassini ion and neutral mass spectrometer. *Geophysical Research Letters, 36*, L08106. https://doi.org/10.1029/2009GL037811

Dalgarno, A. (1958). The mobilities of ions in their parent gases. *Philosophical Transactions Royal Society London, Series A., 250*, 426. https://doi.org/10.1098/rsta.1958.0003

Dialynas, K., Brandt, P. C., Krimigis, S. M., Mitchell, D. G., Hamilton, D. C., Krupp, N. et al. (2013). The extended Saturnian neutral cloud as revealed by global ENA simulations using Cassini/MIMI measurements. *Journal of Geophysical Research, 118*, 3027–3041. https://doi.org/10.1002/jgra.50295

DiFabio, R. D. (2012). Spatial and temporal variations of the suprathermal (3-220 keV/e) ion composition in Saturn's equatorial magnetosphere (Doctoral dissertation). Retrieved from Digital Repository at the University of Maryland, University of Maryland, College Park, Maryland, USA. https://drum.lib.umd.edu/handle/1903/12700

DiFabio, R. D., Hamilton, D. C., Krimigis, S. M., & Mitchell, D. G. (2011). Long term time variations of the suprathermal ions in Saturn's magnetosphere. *Geophysical Research Letters, 38*, L18103. https://doi.org/10.1029/2011GL048841

Dong, Y., Hill, T. W., Teolis, B. D., Magee, B. A., & Waite, J. H. (2011). The water vapor plumes of Enceladus. *Journal of Geophysical Research, 116*, A10204. https://doi.org/10.1029/2011JA016693

Dong, Y., & Hill, T. W. (2013). A study of the charged ice grains in the Enceladus plume with a composite size distribution. American Geophysical Union Fall Meeting, abstract, P32B-04. 2013AGUFM.P32B..04D.

Dong, Y., Hill, T. W., & Ye, S. -Y. (2015). Characteristics of ice grains in the Enceladus plume from Cassini observations. *Journal of Geophysical Research, 120*, 915–937. http://dx.doi.org/10.1002/ 2014JA020288

Dyke, T. R., & Muenter, J. S. (1973). Electric dipole moments of low J states of H2O and D2O. *Journal of Chermical Physics, 59*, 3125-3127. https://doi.org/10.1063/1.1680453

Engelhardt, I. A. D.; Wahlund, J. -E.; Andrews, D. J.; Eriksson, A. I.; Ye, S.; Kurth, W. S.; et al. (2015). Plasma regions, charged dust and field-aligned currents near Enceladus. *Planetary and Space Science, 117*, 453-469. https://doi.org/10.1016/j.pss.2015.09.010

Farmer, A. J. (2009). Saturn in hot water: Viscous evolution of the Enceladus torus. *Icarus, 202*, 280-286. https://doi.org/10.1016/j.icarus.2009.02.031

Fleshman, B. L., Delamere, P. A., & Bagenal, F. (2010a). Modeling the Enceladus plume-plasma interaction. *Geophysical Research Letters, 37*, L03202. https://doi.org/10.1029/2009GL041613.

Fleshman, B. L., Delamere, P. A., & Bagenal, F. (2010b). A sensitivity study of the Enceladus torus. *Journal of Geophysical Research, 115*, E04007. https://doi.org/10.1029/2009JE003372

Fleshman, B. L., Delamere, P. A., Bagenal, F., and Cassidy, T. (2013). A 1-D model of physical chemistry in Saturn's inner magnetosphere. *Journal of Geophysical Research, 118*, 1567–1581. https://doi.org/doi:10.1002/jgre.20106

González-Alfonso, E., Fischer, J., Bruderer, S., Müller, H. S. P., Graciá-Carpio, J., Sturm, E., et al. (2013). Excited OH^+, H_2O^+, and H_3O^+ in NGC 4418 and Arp 220. *Astronomy & Astrophysics, 550*, A25, 1-23. https://doi.org/10.1051/0004-6361/201220466

Hansen, C. J., Esposito, L., Stewart, A. I. F., Colwell, J., Hendrix, A., Pryor, W., Shemansky, D., & West, R. (2006). Enceladus' water vapor plume. *Science, 311*, 1422-1425. https://doi.org/10.1126/science.1121254

Hill, T. W., Rymer, A. M., Burch, J. L., Crary, F. J., Young, D. T., Thomsen, M. F., et al. (2005). Evidence for rotationally driven plasma transport in Saturn's magnetosphere. *Geophysical Research Letters, 32*, L14S10. https://doi.org/10.1029/2005GL022620

Hill, T. W., Thomsen, M. F., Tokar, R. L., Coates, A. J., Lewis, G. R., Young, D. T., et al. (2012). Charged nanograins in the Enceladus plume. *Journal of Geophysical Research, 117*, A05209. https://doi.org/doi:10.1029/2011JA017218

Holmberg, M. K. G., Wahlund, J. -E., & Morooka, M. W. (2014). Dayside/nightside asymmetry of ion densities and velocities in Saturn's inner magnetosphere. *Geophysical Research Letters, 41*, 3717–3723. https://doi.org/10.1016/10.1002/2014GL060229

Holmberg, M. K. G., Wahlund, J. -E., Morooka, M. W., & Persoon, A. M. (2012). Ion densities and velocities in the inner plasma torus of Saturn. *Planetary and Space Science, 73*, 1, 151-160. https://doi.org/10.1016/j.pss.2012.09.016

Holmberg, M. K. G., Shebanits, O., Wahlund, J.-E., Morooka, M., Vigren, E., André, N., et al. (2017). Density structures, dynamics, and seasonal and solar cycle modulations of Saturn's inner plasma disk. *Journal of Geophysical Research, 122*, 12,258-12,273. https://doi.org/10.1002/2017JA024311

Hood, L. L. (1989). Radial diffusion and losses of energetic protons in the 5 to 12 R_S region of Saturn's magnetosphere. *Journal of Geophysical Research, 94*, A7, 8721-8730. https://doi.org/10.1029/JA094iA07p08721

Horányi, M., Juhász, A., & Morfill, G. E. (2008). Large-scale structure of Saturn's E-ring. *Geophysical Research Letters, 35*, L04203. https://doi.org/10.1029/2007GL032726

Ip, W.-H. (1997). On the neutral cloud distribution in the Saturnian magnetosphere. *Icarus, 126*, 42-57. https://doi.org/10.1006/icar.1996.5618

Ip, W. -H. (2000). Thermal plasma composition in Saturn's magnetosphere. *Planetary & Space*

Science., 48, 755-783. https://doi.org/10.1016/S0032-0633(00)00036-2

Jia, Y. -D., Russell, C. T., Khurana, K. K., Ma, Y. J., Kurth, W., & Gombosi, T. I. (2010). Interaction of Saturn's magnetosphere and its moon: 3. Time variation of the Enceladus plume. *Journal of Geophysical Research, 115*, A12243. https://doi.org/10.1029/2010JA015534

Johnson, R. E., Smith, H. T., Tucker, O. J., Liu, M., Burger, M. H., Sittler, et al. (2006). The Enceladus and OH tori at Saturn. *Astrophysical Journal, 644*, L137. https://doi.org/10.1086/505750

Jurac, S., & Richardson, J. D. (2005). A self-consistent model of plasma and neutrals at Saturn: Neutral cloud morphology. J*ournal of Geophysical Research, 110*, A09220. https://doi.org/10.1029/2004JA0106635

Kempf, S., Beckmann, U. Moragas-Klostermeyer, G., Postberg, F., Srama, R., et al. (2008). The E ring in the vicinity of Enceladus I. Spatial distribution and properties of the ring particles. *Icarus, 193*, 420–437. https://doi.org/10.1016/j.icarus.2007.06.027

Kempf, S., Beckmann U., Srama, R., Horanyi, M., Auer, S., & Grun, E. (2006). The electrostatic potential of E ring particles. *Planetary and Space Science, 54*, 999–1006. https://doi.org/10.1016/j.pss.2006.05.012

Kempf, S., Srama, R., Altobelli, N., Auer, S., Tschernjawski, V., Bradley, et al. (2004). Cassini between Earth and asteroid belt: first in-situ charge measurements of interplanetary grains. *Icarus, 171*, 2, 317-335. https://doi.org/10.1016/j.icarus.2004.05.017

Kollmann, P., E. Roussos, C. Paranicas, N. Krupp, C. M. Jackman, E. Kirsch, and K.•H. Glassmeier (2011). Energetic particle phase space densities at Saturn: Cassini observations and interpretations. *Journal of Geophysical Research, 116*, A05222. https://doi.org/10.1029/2010JA016221

Krimigis, S. M., Mitchell, D. G., Hamilton, D. C., Livi, S., Dandouras, J., Jaskulek, et al. (2004).

Magnetospheric Imaging Instrument (MIMI) on the Cassini Mission to Saturn/Titan. *Space Science Reviews, 114,* 233-329. https://doi.org/10.1007/s11214-004-1410-8.

Krimigis, S. M., Mitchell, D. G., Hamilton, D. C., Krupp, N., Livi, S., Roelof, E. C., et al. (2005). Dynamics of Saturn's magnetosphere from MIMI during Cassini's orbital insertion. *Science, 307*, 5713, 1270-1273. https://doi.org/10.1126/science.1105978

Lishawa, C. R., Dressler, R. A., Gardner, J. A., Salter, R. H., & Murad, E. (1990). Cross sections and product kinetic energy analysis of H_2O^+–H_2O collisions at suprathermal energies. *Journal of Chemical Physics, 93*, 3196-3206; https://doi.org/10.1063/1.458852

Livi, R., Goldstein J., Burch, J. L., Crary, F., Rymer, A. M., Mitchell, D. G., & Persoon, A. M. (2014). Multi-instrument analysis of plasma parameters in Saturn's equatorial, inner magnetosphere using corrections for spacecraft potential and penetrating background radiation. *Journal of Geophysical Research, 119*, 3683–3707. https://doi.org/10.1002/2013JA019616

Marcus, Y. (2012). Volumes of aqueous hydrogen and hydroxide ions at 0 to 200 °C. *Journal of Chemical Physics, 137*, 15, 154501-254501-5. https://doi.org/10.1063/1.4758071

Massey, H. S. W. (1949). Collisions between atoms and molecules at ordinary temperatures. *Rep. Progr. Phys., 12*, 248. https://doi.org/10.1088/0034-4885/12/1/311

Mauk, B. H., Saur, J., Mitchell, D. G., Roelof, E. C., Brandt, P. C., Armstrong, T. P., et al. (2005). Energetic particle injections in Saturn's magnetosphere. *Geophysical Research Letters, 32*, L14S05. https://doi.org/10.1029/2005GL022485

Mauk, B. H., Hamilton, D. C., Hill, T. W., Hospodarsky, G. B., Johnson, R. E., Paranicas, C., et al. (2009). Fundamental plasma processes in Saturn's magnetosphere. In M. K. Dougherty, L. W. Esposito, & S. M. Krimigis (Eds.), *Saturn from Cassini-Huygens* (pp. 281-331). B.V: Springer. https://doi.org/10.1007/978-1-4020-9217-6_11

McAndrews, H. J.□, Thomsen, M. F., Arridge, C. S., Jackman, C. M., Wilson, R. J., Henderson,

M. G., & Dougherty, M. K. (2009). Plasma in Saturn's nightside magnetosphere and the implications for global circulation. *Planetary and Space Science, 57* (14-15), 1714. https://doi.org/10/1016/j.pss.2009.03.003

Meier, P., Kriegel, H., Motschmann, U., Schmidt, J., Spahn, F., Hill, T. W., et al. (2014). A model of the spatial and size distribution of Enceladus' dust plume. *Planetary and Space Science, 104*, 216–233. http://dx.doi.org/10.1016/j.pss.2014.09.016

Melin, J., Ortiz, J. V., Martín, I., Velasco A. M., & Lavín, C. (2005). Ground and excited states of the Rydberg radial H3O: Electron propagator and quantum defect analysis. *Journal of Chemistry and Physics, 122*, 23, 234317-234317-7. https://doi.org/10.1063/1.1926286

Melin, H., Shemansky, D. E., & Liu, X. (2009). The distribution of atomic hydrogen and oxygen in the magnetosphere of Saturn. *Planetary and Space Science, 57,* 1743-1753. https://doi.org/10.1016/j.pss.2009.04.014

Mitchell, D. G., Carbary, J. F., Cowley, S. W. H., Hill, T. W., & Zarka, P. (2009a). *The Dynamics of Saturn's magnetosphere.* In M. K. Dougherty, L. W. Esposito, & S. M. Krimigis (Eds.), *Saturn from Cassini-Huygens* (pp. 257-279). B.V: Springer. https://doi.org/10.1007/978-1-4020-9217-6_10

Mitchell, D. G., Krimigis, S. M., Paranicas, C., Brandt, P. C., Carbary, J. F., Roelof, E. C., et al.(2009b). Recurrent energization of plasma in the midnight-to-dawn quadrant of Saturn's magnetosphere and its relationship to auroral UV and radio emissions. *Planetary and Space Science, 57*, 1732. https://doi.org/10.1016/j.pss.2009.04.002

Nemeth, Z., Szego, K., Foldy, L., Kivelson, M. G., Jia, X., Ramer, K. M., et al. (2015). The latitudinal structure of the nightside outer magnetosphere of Saturn as revealed by velocity moments of thermal ions, Annales Geophysicae, 33, 1195–1202. https://doi.org/10.5194/angeo-33-1195-2015

Northcliffe, L. C., & Schilling, R. F. (1970). Range and stopping-power tables for heavy ions. Atomic Data and Nuclear Data Tables, 7, 3-4, 233-463. https://doi.org/10.1016/S0092-640X(70)80016-X

Paranicas, C., Mitchell, D. G., Krimigis, S. M., Hamilton, D. C., Roussos, E., Krupp, N., et al. (2008). Sources and losses of energetic protons in Saturn's magnetosphere. *Icarus197, 2*, 519-525. https://doi.org/10.1016/j.icarus.2008.05.011

Paranicas, C., Mitchell, D. G., Roelof, E. C., Mauk, B. H., Krimigis, S. M., Brandt, P. C., et al. (2007). Energetic electrons injected into Saturn’s neutral cloud. *Geophysical Research Letters, 34*, L02109. https://doi.org/10.1029/2006GL028676

Persoon, A. M., Gurnett, D. A., Leisner, J. S., Kurth, W. S., Groene, J. B, & Faden, J. B. (2013). The plasma density distribution in the inner region of Saturn’s magnetosphere, *Journal of Geophysical Research, 118,* 2970–2974, https://doi.org/10.1002/jgra.50182

Persoon, A. M., Gurnett, D. A., Santolik, O., Kurth, W. S., Faden, J. B., Groene, J. B., et al. (2009). A diffusive equilibrium model for the plasma density in Saturn’s magnetosphere, *Journal of Geophysical Research, 114*, A04211, https://doi.org/10.1029/2008JA013912

Porco, C. C., Helfenstein, P., Thomas, P. C., Ingersoll, A. P, Wisdom, J., West, R., et al. (2006). Cassini observes the active south pole of Enceladus, *Science, 311*, 1393. https://doi.org/10.1126/science.1123013

Press, W. H., Flannery, B. P., Teukolsky, S. A., & Vetterling, W. T. (1989). *Numerical Recipes: The Art of Scientific Computing*, Cambridge University Press, New York

Rapp, D., & W. E. Francis (1962). Charge exchange between gaseous ions and atoms. *Journal Chemical Physics*, 37, 2631. https://doi.org/10.1063/1.1733066

Richardson, J. D. (1998). Thermal plasma and neutral gas in Saturn's magnetosphere. *Reviews of Geophysics, 36*, 501-524. https://doi.org/10.1029/98RG01691

Richardson, J. D., Eviatar, A., McGrath, M. A., & Vasyliunas V. M. (1998). OH in Saturn's magnetosphere: Observations and implications. *Journal of Geophysical Research, 103*, 20245. https://doi.org/10.1029/98JE01127

Rymer, A. M., Mauk, B. H., Hill, T. W., Paranicas, C., André, N., Sittler Jr., E. C., et al. (2007). Electron sources in Saturn's magnetosphere. *Journal of Geophysical Research, 112*, A02201. https://doi.org/10.1029/2006JA012017

Rymer, A. M., Mauk, B. H., Hill, T. W., Paranicas, C., Mitchell, D. G., Coates, A. J., &Young, D. T. (2008). Electron circulation in Saturn's magnetosphere. *Journal of Geophysical Research, 113*, A01201. https://doi.org/10.1029/2007JA012589

Rymer, A. M., Mauk, B. H., Hill, T. W., André, N., Mitchell, D. G., Paranicas, C., et al. (2009). Cassini evidence for rapid interchange transport at Saturn. *Planetary and Space Science, 57*, 1779. https://doi.org/10.1016/j.pss.2009.04.010

Saur, J., N., Schilling, Neubauer, F. M., Strobel, D. F., Simon, S., Dougherty, M. K., et al. (2008). Evidence for temporal variability of Enceladus' gas jets: Modeling of Cassini observations. *Geophysical Research Letters, 35*, L20105. https://doi.org/10.1029/2008GL035811

Schippers, P., Blanc, M., André, N., Dandouras, I., Lewis, G. R., Gilbert, L. K., et al. (2008). Multi-instrument analysis of electron populations in Saturn's magnetosphere. *Journal of Geophysical Research, 113*, A07208. https://doi.org/10.1029/2008JA013098

Sergis, N., Krimigis, S. M., Mitchell, D. G., Hamilton, D. C., Krupp, N., Mauk, B. M., et al. (2007). Ring current at Saturn: Energetic particle pressure in Saturn's equatorial magnetosphere measured with Cassini/MIMI. *Geophysical Research Letters, 34*, L09102. https://doi.org/10.1029/ 2006GL029223

Sergis, N., Krimigis, S. M., Mitchell, D. G., Hamilton, D. C., Krupp, N., Mauk, B. M., et al.

(2009). Energetic particle pressure in Saturn's magnetosphere measured with the Magnetospheric Imaging Instrument on Cassini. *Journal of Geophysical Research, 114*, A02214. https://doi.org/10.1029/2008JA013774

Shemansky, D. E, Matheson, P., Hall, D. T., Hu, H. -Y., & Tripp, T. M. (1993). Detection of the hydroxyl radical in the Saturn magnetosphere. *Nature, 363*, 329-331. https://doi.org/10.1038/363329a0

Sergis, N., Krimigis, S. M., Roelof, E. C., Arridge, C. S., Rymer, A. M., Mitchell, D. G. et al. (2010). Particle pressure, inertial force, and ring current density profiles in the magnetosphere of Saturn, based on Cassini measurements. *Geophysical Research Letters, 37*, L02102. https://doi.org/10.1029/2009GL041920

Showalter, M. R., Cuzzi, J. N, Larson, S. M. (1991). Structure and particle properties of Saturn's E Ring. *Icarus, 94*, 2, 451-473. https://doi.org/10.1016/0019-1035(91)90241-K

Sittler Jr., E. C., Andre, N., Blanc, M., Burger, M., Johnson, R. E., Coates, A., et al. (2008). Ion and neutral sources and sinks within Saturn's inner magnetosphere: Cassini results. *Planetary and Space Science, 56*, 3. https://doi.org/10.1016/j.pss.2007.06.006

Slater, J. C., (1964). Atomic Radii in Crystals. *Journal of Chemical Physics, 41*, 10, 3199-3204. https://org/doi/10.1063/1.1725697

Smith, H. T., Johnson, R. E., Perry, Mitchell, M. E., D. G., McNutt, R. L., & Young, D. T. (2010). Enceladus plume variability and the neutral gas densities in Saturn's magnetosphere. *Journal of Geophysical Research 115*, A10252. https://doi.org/10.1029/2009JA015184

Srama, R., Ahrens, T. J., Altobelli, N., Auer, S., Bradley, J. G., Burton, M., et al. (2004). The Cassini Cosmic Dust Analyzer. Space Science Reviews, 114, 1-4, 465-518. https://doi.org/10.1007/s11214-004-1435-z

Srama, R., Kempf, S., Moragas-Klostermeyer, G., Altobelli, N., Auer, S., Beckmann, U., et al. (2011). The cosmic dust analyser onboard Cassini: ten years of discoveries. *CEAS Space Journal, 2*, 1-4, 3-16. https://doi.org/10.1007/s12567-011-0014-x

Thomsen, M. F., Reisenfeld, D. B., Delapp, D. M., Tokar, R. L.,Young, D.T., Crary, F. J., et al. (2010). Survey of ion plasma parameters in Saturn's magnetosphere. *Journal of Geophysical Research, 115*, A10220. https://doi.org/10.1029/2010JA015267

Tokar, R. L., Johnson, R. E., Hill, T. W., Pontius, D. H., Kurth, W. S., Crary, F. J., et al. (2006). The interaction of the atmosphere of Enceladus with Saturn's plasma. *Science, 311*, 1409. https://doi.org/10.1126/science.1121061

Tokar, R. L., Johnson, R. E., Thomsen, M. F., Wilson, R. J., Young, D. T., Crary, et al. (2009). Cassini detection of Enceladus' cold water-group plume ionosphere. *Geophysical Research Letters, 36*, L13203. https://doi.org/10.1029/2009GL038923

Van Allen, J. A., Randall, B. A., & Thomsen, M. F. (1980). Sources and sinks of energetic electrons and protons in Saturn's magnetosphere. *Journal of Geophysical Research, 85*, 5679-5694. https://doi.org/10.1029/JA085iA11p05679

Vandegriff, J., DiFabio, R., Hamilton, D., Kusterer, M., Manweiler, J., Mitchell, D., et al. (2018). Cassini/MIMI Instrument Data User Guide. NASA, Washington, D. C. Available at http://pds.nasa.gov

von Steiger, R., Schwadron, N. A., Fisk, L. A., Geiss, J., Gloeckler, G., Hefti, et al. (2000). Composition of quasi-stationary solar wind flows from Ulysses/Solar Wind Ion Composition Spectrometer. *Journal of Geophysical Research, 105*, 27,217-27,238. https://doi.org/10.1029/1999JA000358

Waite Jr., J. H., Combi, M. R., Ip, W. -H., Cravens, T. E., McNutt Jr., R. L., Kasprzak, W., et al.(2006). Cassini ion and neutral mass spectrometer: Enceladus plume composition and structure. *Science, 311*, 1419-1422. https://doi.org/10.1126/science1121290

Walt, M. (1971). The radial diffusion of trapped particles induced by fluctuating magnetospheric fields. *Space Science Reviews, 12, 4*, 446-485. https://doi.org/10.1007/BF00171975

Weast, R. C. (Ed.) (1968). *CRC Handbook of Chemistry and Physics, 49th Ed.*, p. E-71, Cleveland.

Weis, B., Carter, S., Rosmus, P., Werner, H.-J., & Knowles, P. J. (1989). A theoretical rotationally resolved infrared spectrum for H_20^+ (X 28 1). *Journal of Chemical Physics, 91*, 2818-2833. https://doi.org/10.1063/1.456951

Werner, H.-J., Rosmus, P., & Reinsch, E.-A. (1983). Molecular properties from MCSCF-SCEP wave functions. I. Accurate dipole moment functions of OH, OH^-, and OH^+. *Journal of Chemical Physics, 79*, 905-916. https://doi.org/10.1063/1.445867

Wiedmann, R. T., Tonkyn, R. G., White, M. G., Kwanghsi, W., & McKoy, V. (1992). Rotationally resolved threshold photoelectron spectra of OH and OD. *Journal Chemical Physics, 97*, 768-772. https://doi.org/10.1063/1.463179

Wilson, R. J., Bagenal, F., Cassidy, T., Fleshman, B. L., &. Crary, F. (2015), The relative proportions of water group ions in Saturn's inner magnetosphere: A preliminary study, *Journal Geophysical Research, Space Physics, 120*, 6624–6632,https://doi.org/10.1002/2014JA020557

Wilson, R. J., Tokar, M. G., Henderson, R. L., Hill, T. W, Thomsen M. F., & Pontius, D. H. (2008). Cassini plasma spectrometer thermal ion measurements in Saturn's inner magnetosphere. *Journal of Geophysical Research, 113*, A12218. https://doi.org/10.1029/2008JA013486

Ye, S.-Y., Gurnett, D. A., Kurth, W. S., Averkamp, T. F., Kempf, S., Hsu, H.-W., Srama, R., & Grün, E. (2014). Properties of dust particles near Saturn inferred from voltage pulses induced by dust impacts on Cassini spacecraft. *Journal of Geophysical Research, 119*, 6294–6312.

https://doi.org/10.1002/ 2014JA020024

Young, D. T., Berthelier, J.-J., Blanc, M., Burch, J. L., Bolton, S., Coates, A. J., et al. (2005). Composition and dynamics of plasma in Saturn's magnetosphere. *Science, 307*, 1262-1266. https://doi.org/10.1126/science.1106151

Ye, S.-Y., D. A. Gurnett, W. S. Kurth, T. F. Averkamp, S. Kempf, H.-W. Hsu, R. Srama, and E. Grün (2014), Properties of dust particles near Saturn inferred from voltage pulses induced by dust impacts on Cassini spacecraft, J. Geophys. Res. Space Physics, 119, 6294–6312, doi:10.1002/ 2014JA020024

Ye, S.-Y., W. S. Kurth, G. B. Hospodarsky, T. F. Averkamp, and D. A. Gurnett (2016). Dust detection in space using the monopole and dipole electric field antennas, J. Geophys. Res. Space Physics, 121, 11,964–11,972. doi:10.1002/ 2016JA023266.

Acknowledgements. This research was supported in part by the NASA Office of Space Science under Task Order 003 of contract NAS5-97271 between NASA Goddard Space flight Center and the Johns Hopkins University. Participation at JHU/APL and the University of Maryland was also funded in part by NASA Grant NNX07AJ69G. The entire Cassini/MIMI/CHEMS data set and Cassini ephemeris data are publicly available in the Planetary Data System and can be found at http://pds.nasa.gov. We thank M. Chaplin for useful discussions.

Figure Captions

Figure 1. (a) Essd channel, the Solid State Detector (SSD) energy channel number, versus TOF channel, the time-of-flight channel number of the ~96 keV W^+. (b) The ~96 keV W^+ TOF channel count histogram for the data in the Essd channel range indicated by the horizontal red dashed lines in (a). Data from 78 equatorial ring current passes from 2004 to 2010 are summed. These data are from CHEMS telescope 1 which has the best heavy ion resolution (DiFabio, 2012).

Figure 2. ~96 keV O^{++} (E/Q = 48 keV/e) TOF Channel count distribution for all 78 equatorial ring current passes from 2004 to 2010 (L = 7-16, Latitude = -10° to 10°) combined. The solid red line represents the best fit to the distribution using Equation 1 (See text). We use an asymmetric Gaussian to fit the counts near the center of the distribution and add a small correction to the Gaussian on the right side to fit the counts in the "tail."

Figure 3. Best fit of the ~96 keV W^+ distribution. The fits to each individual species are shown along with the sum of the four fits (red). The data are from CHEMS telescope 1.

Figure 4. (a) The partial number density of energetic, 96 keV, water group components versus L. (b) The fractional abundance of 96 keV water group components versus L. The error bars of O^+, OH^+, and H_2O^+ represent the statistical uncertainties from the best fit. The error bars of H_3O^+ represent the spread of values from our three different fits (see text).

Figure 5. (top 3 panels) The water-group fractional abundances plotted over model E-ring grain (Hornáyi et al., 2008) and OH density (Jurac et al., 2005) information. (bottom panel) Grain charge information from Kempf et al. (2008) and Ye et al. (2014).

Equations 1 (top) and 2 (bottom)

$$f(\tau) = A\left[e^{-\frac{(\tau-\tau_c)^2}{2\sigma_1{}^2}} P(-\tau+\tau_c) + \left(e^{-\frac{(\tau-\tau_c)^2}{2\sigma_2{}^2}} + \frac{(\tau-\tau_c)^2}{100+\left[(\tau-\tau_c)^2\right]^{\alpha}}\right) P(\tau-\tau_c)\right] \tag{1}$$

$$v_{\max} = \frac{v_o\,|\Delta E|}{h} \tag{2}$$

Table 1: Partial number density and relative abundance of the four major ~96 keV W^+ components in Saturn's equatorial ring current region (L = 7-16)[a].

Species	Counts	Partial Number Density ($\times10^{-6}$ cm^{-3})	Fraction of W^+
O^+	14400	23.4 ± 0.7	0.53 ± 0.02
OH^+	5743	9.6 ± 0.4	0.22 ± 0.01
H_2O^+	5607	9.7 ± 0.4	0.22 ± 0.01
H_3O^+	690	1.2 +0.4, -0.48[b]	0.028 +0.01, -0.012[b]

a The abundances are determined using the results from our best fit (α = 1.90). The uncertainties of O^+, OH^+, and H_2O^+ reflect the statistical uncertainties from our fits.

b The H_3O^+ uncertainty reflects the range of values from our three fits (see text).

Table 2: Component to Total* W^+ Fractional Abundance Ratio Comparisons

W^+ Analysis	O^+/W^+	OH^+/W^+	H_2O^+/W^+	H_3O^+/W^+
This Study (Suprathermal Ions) ($\sim 7 \leq L \leq \sim 16$)	0.52-0.55	0.20-0.22	0.22-0.22	0.047-0.023
Wilson et al. (2015) (Thermal Ions) ($\sim 7 \leq L \leq \sim 10$)	0.20-0.24	0.28-0.30	0.29-0.28	0.23-0.18
Fleshman et al. (2013) (Model) ($\sim 7 \leq L \leq \sim 10$)	0.24-0.33	0.19-0.22	0.29-0.26	0.28-0.19

* $[W^+] = [O^+] + [OH^+] + [H_2O^+] + [H_3O^+]$, the W^+ population is the sum of the O^+, OH^+, H_2O^+, and H_3O^+ populations

Figure 1.

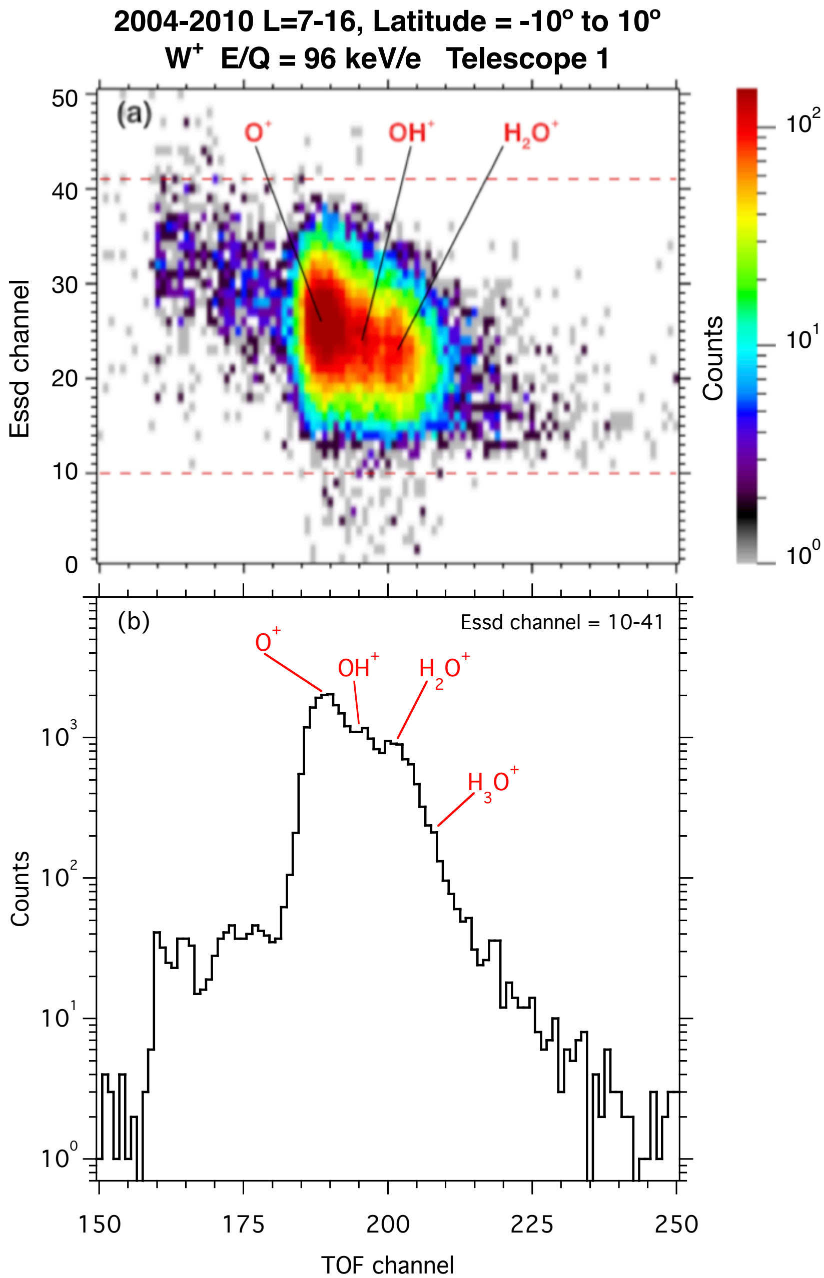

2004-2010 L=7-16, Latitude = -10° to 10°
W+ E/Q = 96 keV/e Telescope 1
(a)
O+
OH+
H2O+
Essd channel
Counts
(b)
Essd channel = 10-41
O+
OH+
H2O+
H3O+
Counts
TOF channel

Figure 2.

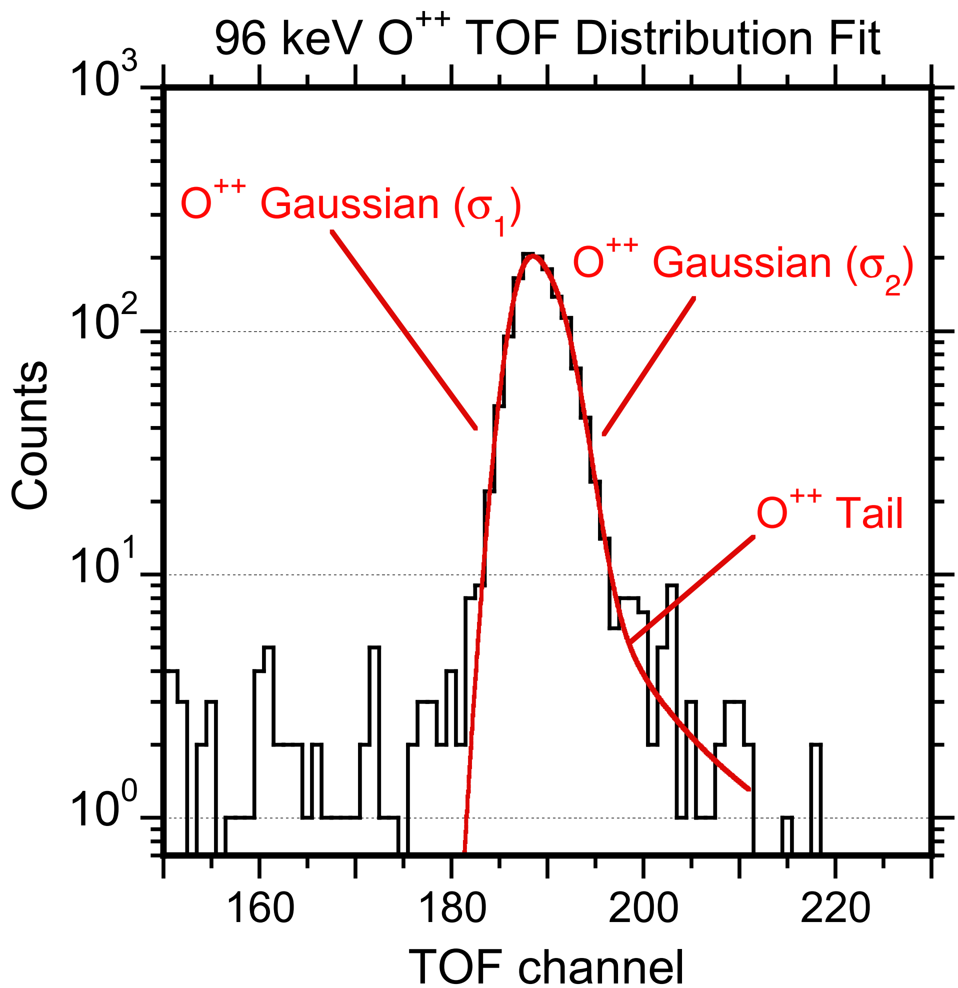
96 keV O++ TOF Distribution Fit
Counts
TOF channel
10^3
10^2
10^1
10^0
160
180
200
220
O++ Gaussian (σ1)
O++ Gaussian (σ2)
O++ Tail

Figure 3.

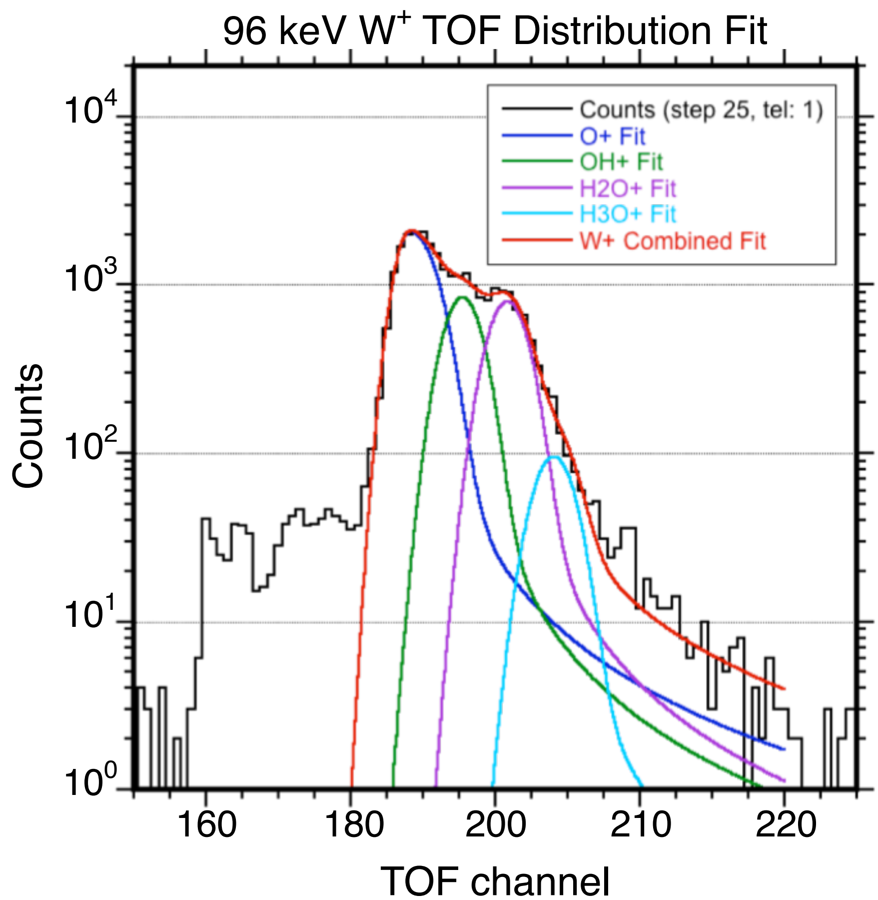

96 keV W+ TOF Distribution Fit
Counts (step 25, tel: 1)
O+ Fit
OH+ Fit
H2O+ Fit
H3O+ Fit
W+ Combined Fit
Counts
TOF channel
10^4
10^3
10^2
10^1
10^0
160
180
200
210
220

Figure 4.

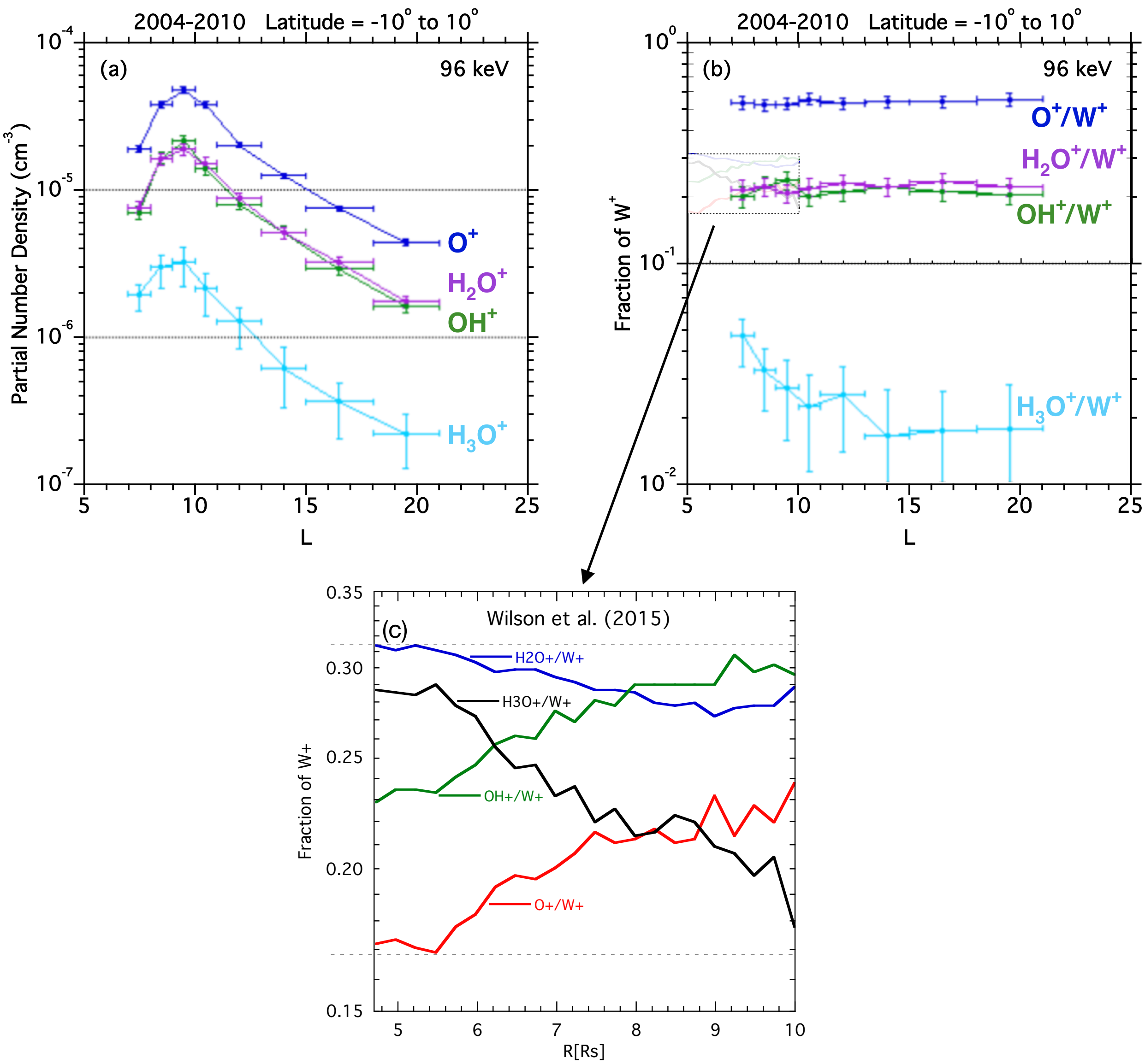

2004-2010 Latitude = -10° to 10°
(a)
96 keV
Partial Number Density (cm⁻³)
O+
H2O+
OH+
H3O+
L
2004-2010 Latitude = -10° to 10°
(b)
96 keV
Fraction of W+
O+/W+
H2O+/W+
OH+/W+
H3O+/W+
L
Wilson et al. (2015)
(c)
H2O+/W+
H3O+/W+
OH+/W+
O+/W+
Fraction of W+
R[Rs]

Figure 5.

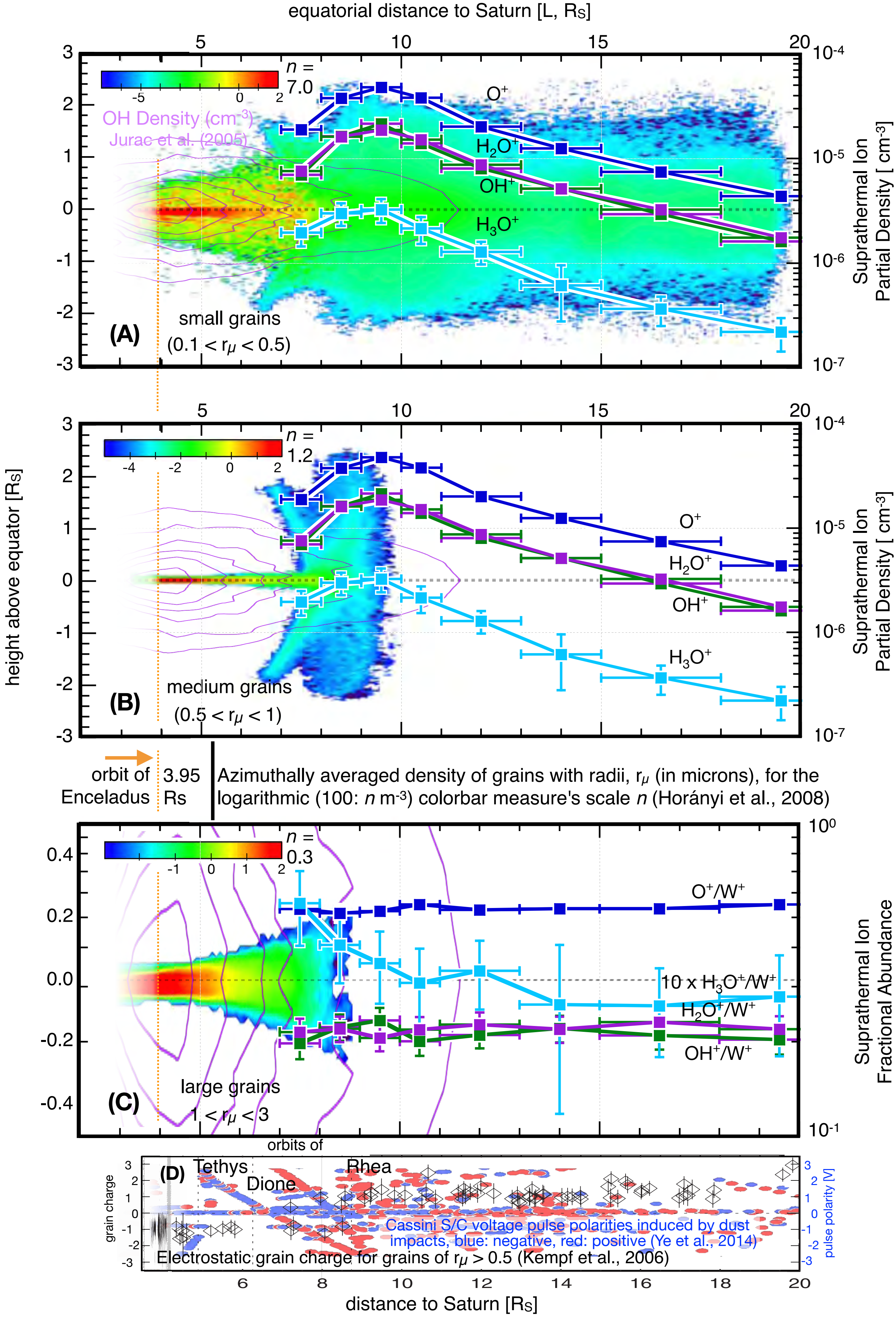

equatorial distance to Saturn [L, Rs]
n = 7.0
OH Density (cm-3)
Jurac et al. (2005)
O+
H2O+
OH+
H3O+
small grains
(0.1 < rμ < 0.5)
(A)
Suprathermal Ion
Partial Density [cm-3]
n = 1.2
medium grains
(0.5 < rμ < 1)
(B)
height above equator [Rs]
orbit of Enceladus
3.95 Rs
Azimuthally averaged density of grains with radii, rμ (in microns), for the logarithmic (100: n m-3) colorbar measure's scale n (Horányi et al., 2008)
n = 0.3
O+/W+
10 x H3O+/W+
H2O+/W+
OH+/W+
large grains
1 < rμ < 3
(C)
Suprathermal Ion
Fractional Abundance
orbits of
Tethys
Dione
Rhea
(D)
grain charge
pulse polarity [V]
Cassini S/C voltage pulse polarities induced by dust impacts, blue: negative, red: positive (Ye et al., 2014)
Electrostatic grain charge for grains of rμ > 0.5 (Kempf et al., 2006)
distance to Saturn [Rs]

Journal of Geophysical Research, Space Physics

Supporting Information for

The Composition of 96 keV W^+ in Saturn's Magnetosphere

R. D. DiFabio[1,2], D. C. Hamilton[1], S. P. Christon[3*], D. G. Mitchell[4], S. M. Krimigis[4,5]

1. University of Maryland, Department of Physics, College Park, MD, USA
2. now at : University of Louisiana, Department of Physics, Lafayette, LA, USA
3. Focused Analysis and Research, Charleston, SC, USA
4. Johns Hopkins University, Applied Physics Laboratory, Laurel, MD, USA
5. Academy of Athens, Athens, Greece

Contents of this file

Table S1. Molecular Ionic Radius and Diameter Information

		Radius, r_I		Diameter		Reference
H_3O^+	hydroxonium (hydronium)	0.100 nm	= 100.0 pm	0.200 nm	= 200.0 pm	(MCa;Marcus, 2012)
H_2O^+	water ion	0.138 nm	= 138.0 pm	0.276 nm	= 276.0 pm	(MCa)
H_2O^o	water(diameter)	1.38 Å	= 138.0 pm	2.75 Å	= 275.0 pm	(MCc)
OH^+	hydroxyl	1.032 Å	= 103.2 pm	2.064 Å	= 206.4 pm	(NIST)
OH^-	r_{OH-} (r_{OHo} ± 0.002 A)		= 103.7 pm		= 207.4 pm	(Branscomb, 1966)
OH^-	hydroxide	0.970 Å	= 97.0 pm	1.94 Å	= 194.0 pm	(NIST)
OH^-		0.110 nm	= 110.0 pm	0.220 nm	= 220.0 pm	(MCb)
OH^o	hydroxyl radical		= 103.5 pm		= 207.0 pm	(average: OH^+,OH^-)
O^o	oxygen atom	60pm	= 60.0 pm		= 120.0 pm	(Slater, 1964)

References:

Chaplin, M. (2019), Water Structure and Science, London South Bank University (http://www1.lsbu.ac.uk/water/water_structure_science.html).

MCa: Chaplin19a: http://www1.lsbu.ac.uk/water/hydrogen_ions.html

MCa: "H_3O^+ has an effective ion radius of 0.100 nm, ... less than that of the H_2O molecular radius (0.138 nm)."

MCb: Chaplin19b: http://www1.lsbu.ac.uk/water/ionisoh.html

MCc: http://www1.lsbu.ac.uk/water/water_molecule.html

Marcus, Y. (2012). Volumes of aqueous hydrogen and hydroxide ions at 0 to 200 °C. *Journal of Chemical Physics, 137*, 15, 154501-254501-5. https://doi.org/10.1063/1.4758071

Branscomb, L. M., (1966). Photodetachment cross section, electron affinity, and structure of the negative hydroxyl ion. *Physical Review, 148*, 1, 11-18. https://org/doi/10.1103/PhysRev.148.11

Slater, J. C., (1964). Atomic Radii in Crystals. *Journal of Chemical Physics, 41*, 10, 3199-3204. https://org/doi/10.1063/1.1725697

Figure 4 of Cassidy & Johnson (2010): neutral density at Rhea's orbital distance

(a) O-density(at Rhea) ~70/cc

(a) $r_I+r_N(O\_H_2O^+)$ = (138+60)e-12 = 198e-12

$(r_{I+}r_N)^2 N_N$ = (198e-12 m)^2 x 70/cc

→→ $(r_{I+}r_N)^2 N_N$ = 2.7e-18

(b) OH-density(at Rhea) ~20/cc

(b) r_I+r_N $(OH\_H_2O^+)$ = (138+97)e-12 = 235e-12

$(r_{I+}r_N)^2 N_N$ = (235e-12 m)^2 x 20/cc

→→ $(r_{I+}r_N)^2 N_N$ = 1.1e-18

Figure 6 of Smith et al. (2010): neutral density at Rhea's orbital distance, average of Cassini E3 and E5 flybys

(c) O-density(at Rhea) ~100/cc

(c) $r_I+r_N(O\_H_2O^+)$ = (138+60)e-12 = 198e-12

$(r_{I+}r_N)^2 N_N$ = (198e-12 m)^2 x 100/cc

→→ $(r_{I+}r_N)^2 N_N$ = 3.9e-18

(d) OH-density(at Rhea) ~50/cc

(d) $r_I+r_N(O\_H_2O^+)$ = 138+97 = 235e-12

$(r_{I+}r_N)^2 N_N$ = (235e-12 m)^2 x 50/cc

→→ $(r_{I+}r_N)^2 N_N$ = 2.8e-18

Table S2. Grain Size and Density Information

Srama et al. (2011): give $n(r) = 20(r - 2.8)^{-4.6}$ for grain density falloff (best fit at 3.95-8.73 R_s)
Enceladus: $20\,(3.95 - 2.8)^{-4.6} = 10.515258$: 10.5
Rhea: $20\,(8.73 - 2.8)^{-4.6} = 0.005559.$: 5.56e-3
Grain/dust density scale factor: 0.005559/10.515258 = 0.000529 ~ 5e-4
(e) grain size = 1.0 nm = 0.3e-9 = 1000e-12 m, from Fig.10, Dong et al. (2015)
(f) grain size = 2.0 nm = 2.0e-9 = 2000e-12 m, from Fig.10, Dong et al. (2015)
grain density@Rhea = 2000 x 5e-4 = 1, from Fig.11a, Dong et al. (2015); Fig.11,Srama et al. (2011)
(e) 1.0 nm grains: r_I+r_G = 138 + 1000 = 1138e-12
$(r_{I+}r_G)^2\,N_{G(1)}$ = $(1138e\text{-}12)^2$ * 2000 * (1) * 5e-4
→→ $(r_{I+}r_G)^2\,N_{G(1)}$ = 1.3e -18
(f) 2.0 nm grains: r_I+r_G = 138 + 2000 = 2138e-12
$(r_{I+}r_G)^2\,N_{G(2)}$ = $(2138e\text{-}12)^2$ * 1000 * (1) * 5e-4
→→ $(r_{I+}r_G)^2\,N_{G(2)}$ = 2.3e-18
(g) 4.0 nm grains: r_I+r_G = 138 + 4000 = 4138e-12
$(r_{I+}r_G)\,N_{G(4)}$ = $(4138e\text{-}12)^2$ * 200 * (1) * 5e-4
→→ $(r_{I+}r_G)\,N_{G(4)}$ = 1.7e-18

Table S3. Mean Free Path Ratio ($\boldsymbol{\Gamma}_{N:G}$) Calculations for H_2O^+ in neutral gas (a-d) and grains (e,f) †

--------(*::e, 1 nm)---------------	--------(*::f, 2 nm)---------------	--------(*::g, 4 nm)---------------
a: 1.3e-18/2.7e-18 = 4.81e-1	a: 2.3e-18/2.7e-18 = 8.52e-1	a: 1.7e-18/2.7e-18 = 6.29e-1
b: 1.3e-18/1.1e-18 = 1.18e0	b: 2.3e-18/1.1e-18 = 2.09e0	b: 1.7e-18/1.1e-18 = 1.55e0
c: 1.3e-18/3.9e-18 = 3.33e-1	a: 2.3e-18/3.9e-18 = 5.90e-1	a: 1.7e-18/3.9e-18 = 4.36e-1
d: 1.3e-18/2.8e-18 = 4.64e-1	b: 2.3e-18/2.8e-18 = 8.21e-1	b: 1.7e-18/2.8e-18 = 6.07e-1

or roughly,

a: [O] ~ [1 nm] ~ 0.48 ~ 1/2	a: [O] ~ [2 nm] ~ 0.85 ~ 1	a: [O] ~ [4 nm] ~ 0.63 ~ 1/2
b: [OH] ~ [1 nm] ~ 1.2 ~ 1	b: [OH] ~ [2 nm] ~ 2 ~ 2	b: [OH] ~ [4 nm] ~ 1.6 ~ 1 1/2
c: [O] ~ [1 nm] ~ 0.33 ~ 1/3	c: [O] ~ [2 nm] ~ 0.6 ~ 1/2	c: [O] ~ [4 nm] ~ 0.44 ~ 1/2
d: [OH] ~ [1 nm] ~ 0.46 ~ 1/2	d: [OH] ~ [2 nm] ~ 0.8 ~ 1	d: [OH] ~ [4 nm] ~ 0.61 ~ 1/2

† https://chem.libretexts.org/Bookshelves/Physical_and_Theoretical_Chemistry_Textbook_Maps/Book%3A_Thermodynamics_and_Chemical_Equilibrium_(Ellgen)/04%3A_The_Distribution_of_Gas_Velocities/4.12%3A_The_Frequency_of_Collisions_between_Unlike_Gas_Molecules

Sample Calculation for a::e at Rhea:

A_N = (198e-12 m)^2 $\qquad$ A_G = (1138e-12 m)^2
N_N = 70/cc $\qquad$ N_G = 2000 * 5e-4

$$\boldsymbol{\Gamma}_{N:G} = \frac{N_G \times A_G}{N_N \times A_N} = \frac{2000 \times 5e\text{-}4 \;\times (1138e\text{-}12\ m)^2}{70. \qquad \times (198e\text{-}12\ m)^2} = \frac{1.295e\text{-}18}{2.744e\text{-}18} \sim \frac{1.3}{2.7} = 0.48$$

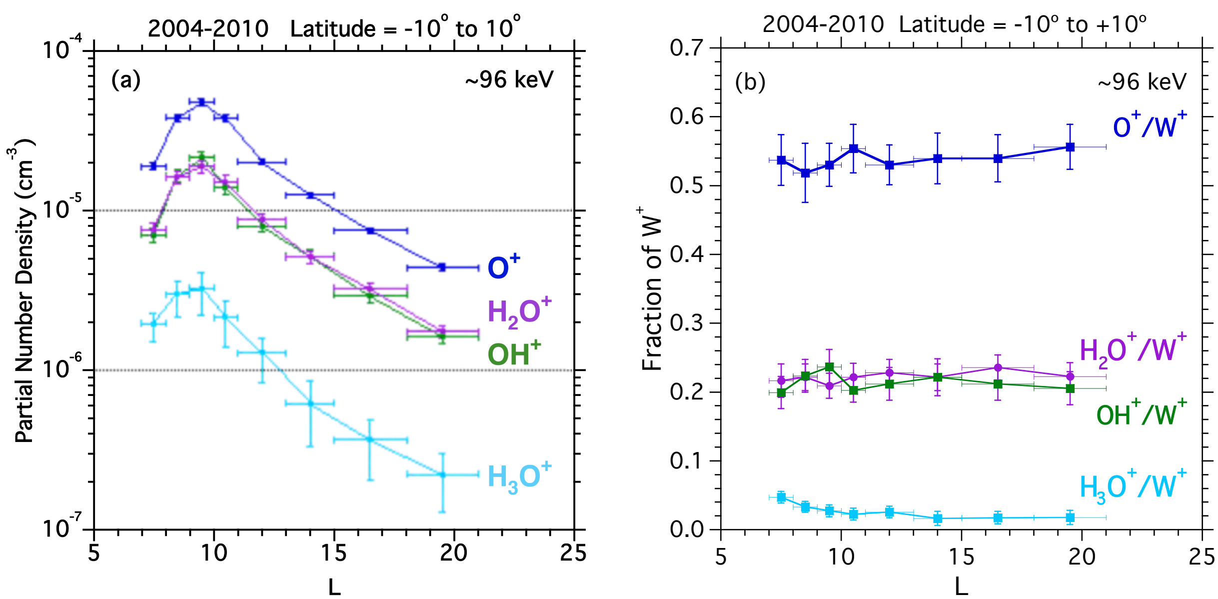

Figure S1 (see Figure 4). (a) The partial number density of energetic, ~96 keV, water group components versus L. (b) The fractional abundance of ~96 keV water group components plotted linearly versus L. The error bars of O^+, OH^+, and H_2O^+ represent the statistical uncertainties from the best fit. The error bars of H_3O^+ represent the spread of values from our three different fits (see text).

Figure S2. Figure 5 from Paranicas et al. (2008)

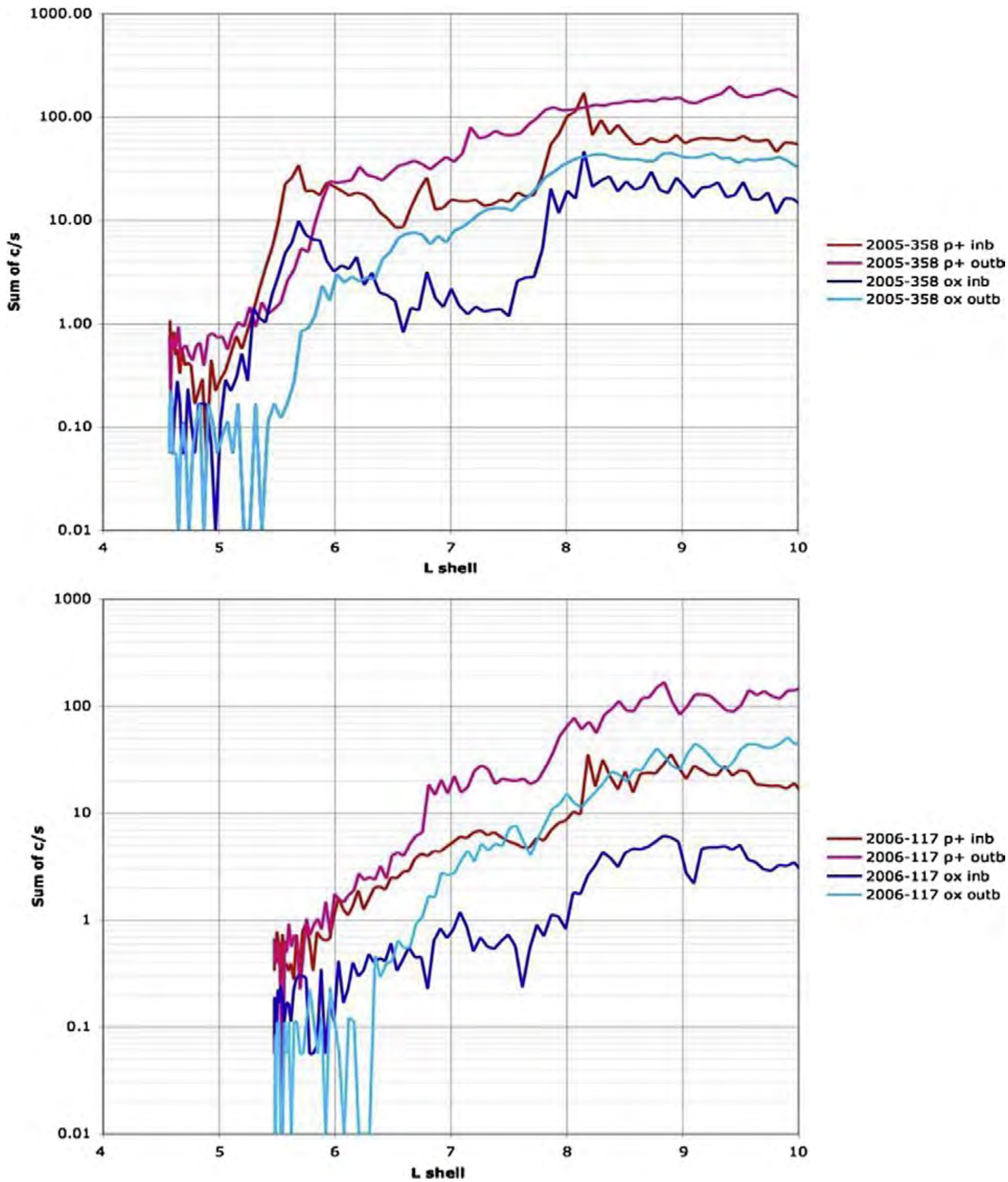

Fig. 5. Summed count rates for the periods in Fig. 3 (top) and Fig. 4 (bottom). The inbound and outbound data are plotted separately with the proton sum red and the oxygen sum blue. The proton (oxygen) sum is over the CHEMS energy range 3–220 (8–220) keV.

Figure S3. Figure 1 from Kollmann et al. (2011)

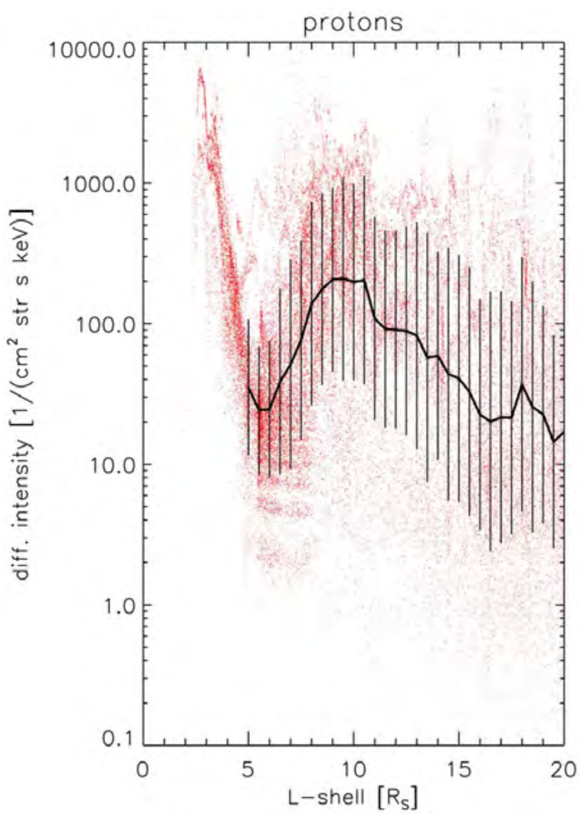

Figure 1. Differential intensities $\bar{j}$ of (left) protons and (right) electrons. Protons have mean energies of 46 keV, and electrons have mean energies of 91 keV; both species have equatorial pitch angles of α_0 = 10° ± 10°. The red points represent single measurements taken between July 2004 and June 2010 (with exceptions, see section 2). The black solid line is the logarithmic average of these points within intervals of 0.5 R_S width. Error bars show the associated 1σ standard deviations. The increase of intensities for $L < 5$ is caused by penetrating background and does not represent particles at the mentioned energies.

Figure S4. Figure 4 from Christon et al. (2014)

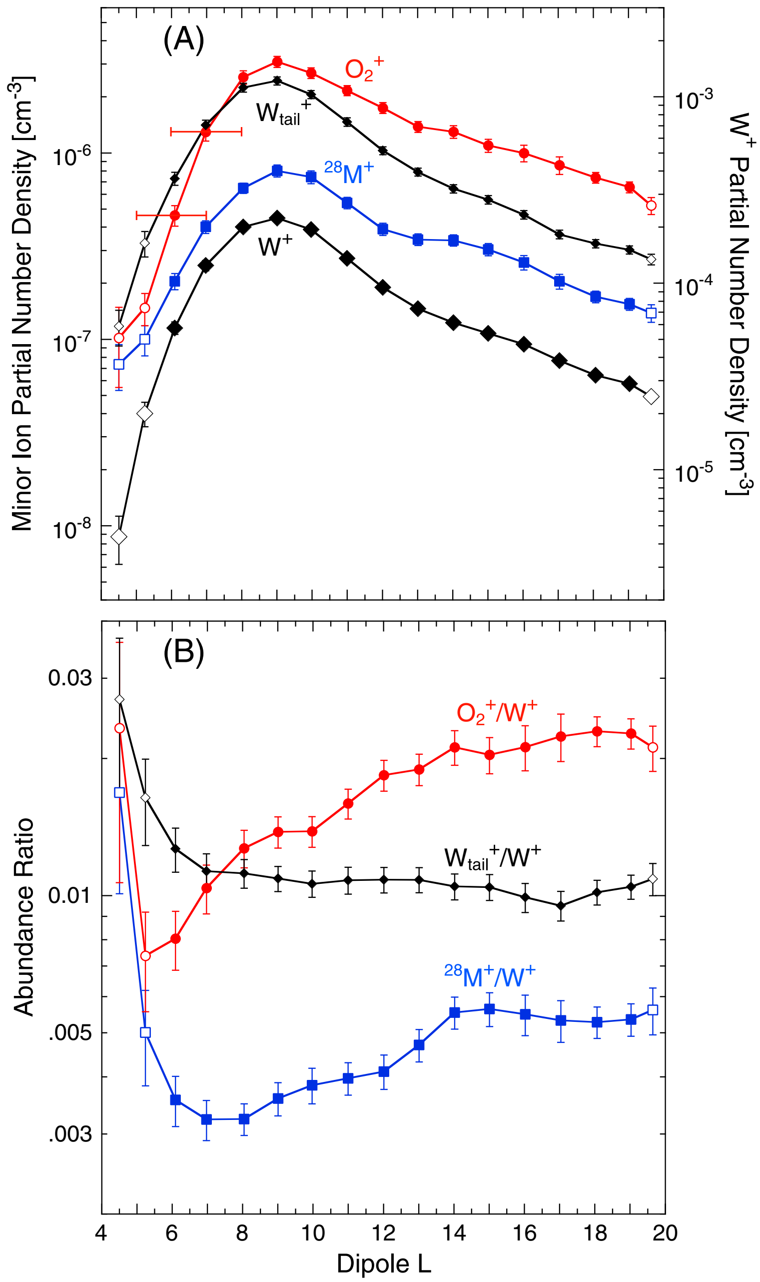

Figure 4. Running dipole L averages stepped every integer L value (with a 2 R_S window) of (a) W^+ and minor ion partial number densities, PNDs, where the right-side scale for W^+ is offset by several orders of magnitude to facilitate comparison with the minor ions and (b) abundance ratios of minor ions relative to W^+. The running averages are collected on strict integer L bounds and plotted at the mean distance of the average. Uncertainties shown are standard error of the means for ease of statistical comparison. Open symbols at $L < 6$ identify data currently undersampled when compared to the other L intervals. Open symbols at $L > 19$ identify data that may be affected by proximity to the magnetopause.

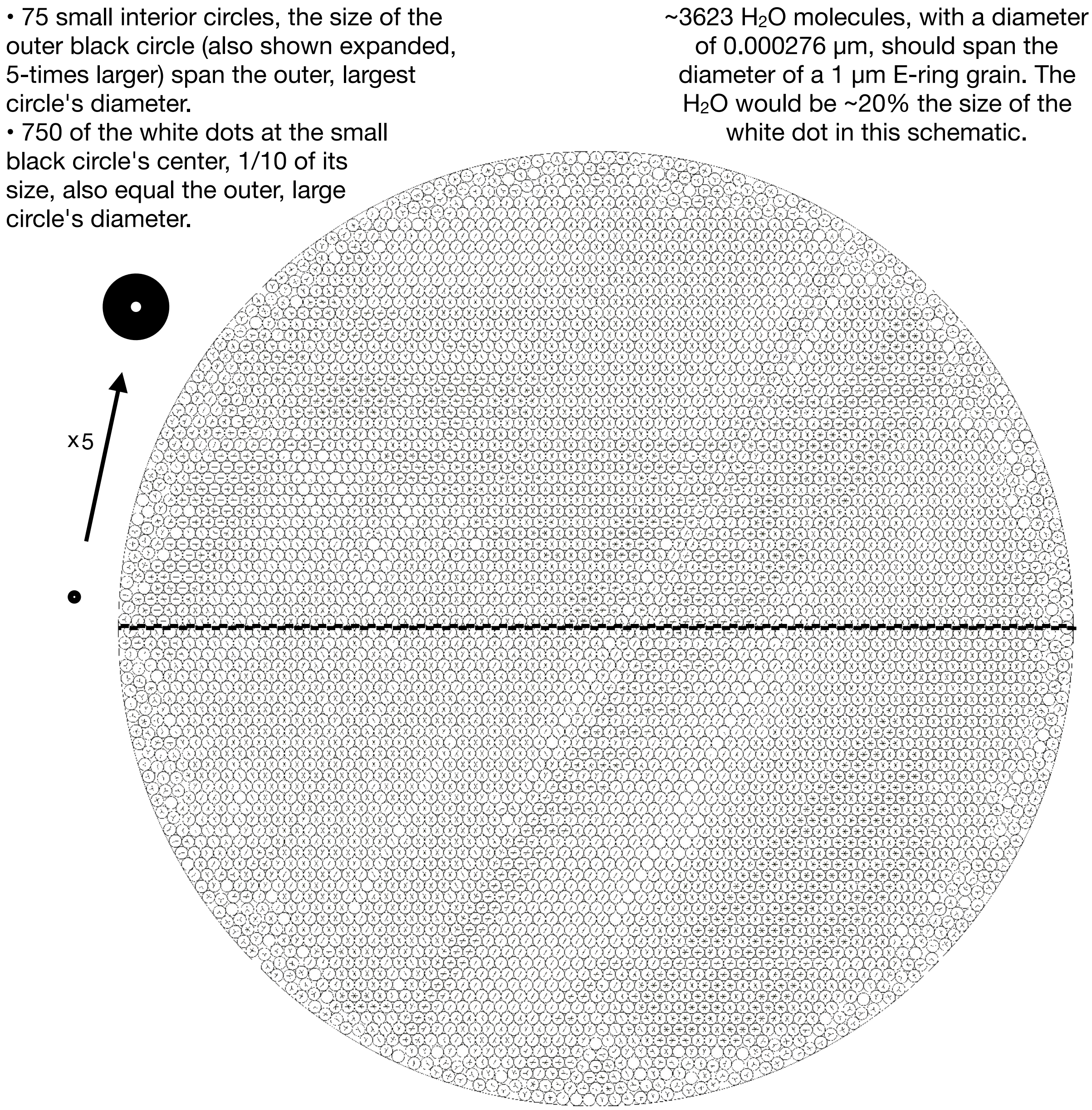

Figure S5. In order to visualize relevant ion-grain cross section scale sizes, we show an example of a large circle packed with 5000 small circles (E. Specht, 2018, The best known packings of equal circles in a circle, http://hydra.nat.uni-magdeburg.de/packing/cci/cci.html#cci5000) to represent a 1 µm E-ring grain. These interior circles are the same size as the exterior black circle that represents an enlarged version of a H_2O^+ molecule propagating into the E-ring region. An actual H_2O relative to a 1 µm E-ring grain is ~20% smaller in this comparison than the white dot size shown. Other E-ring targets are the OH molecular ions and both larger and smaller dust grains, charged both positively and negatively inside ~9 Rs (near the orbit of Rhea).